

## NO Reduction to N<sub>2</sub>O Triggered by a Dinuclear Dinitrosyl Iron Complex via the Associated Pathways of Hyponitrite Formation and NO Disproportionation

Wun-Yan Wu, Ming-Li Tsai,\* Yi-An Lai, Chieh-Hsin Hsieh, and Wen-Feng Liaw\*

Cite This: <https://doi.org/10.1021/acs.inorgchem.1c00541>

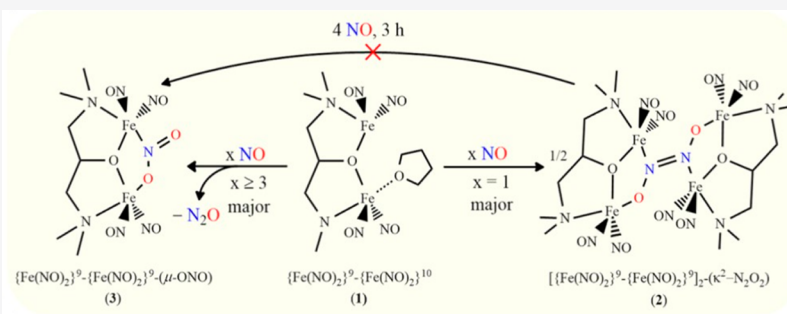
Read Online

ACCESS |

Metrics & More

Article Recommendations

Supporting Information



**ABSTRACT:** In spite of the comprehensive study of the metal-mediated conversion of NO to N<sub>2</sub>O disclosing the conceivable processes/mechanism in biological and biomimetic studies, in this study, the synthesis cycles and mechanism of NO reduction to N<sub>2</sub>O triggered by the electronically localized dinuclear {Fe(NO)<sub>2</sub>}<sup>10</sup>-{Fe(NO)<sub>2</sub>}<sup>9</sup> dinitrosyl iron complex (DNIC) [Fe(NO)<sub>2</sub>(μ-bdmap)Fe(NO)<sub>2</sub>(THF)] (1) (bdmap = 1,3-bis(dimethylamino)-2-propanolate) were investigated in detail. Reductive conversion of NO to N<sub>2</sub>O triggered by complex 1 in the presence of exogenous ·NO occurs via the simultaneous formation of hyponitrite-bound [{Fe<sub>2</sub>(NO)<sub>4</sub>(μ-bdmap)]<sub>2</sub>(κ<sup>2</sup>-N<sub>2</sub>O<sub>2</sub>) (2) and [NO<sub>2</sub>]<sup>-</sup>-bridged [Fe<sub>2</sub>(NO)<sub>4</sub>(μ-bdmap)(μ-NO<sub>2</sub>)] (3) (NO disproportionation yielding N<sub>2</sub>O and complex 3). EPR/IR spectra, single-crystal X-ray diffraction, and the electrochemical study uncover the reversible redox transformation of {Fe(NO)<sub>2</sub>}<sup>9</sup>-{Fe(NO)<sub>2</sub>}<sup>9</sup> [Fe<sub>2</sub>(NO)<sub>4</sub>(μ-bdmap)(μ-OC<sub>4</sub>H<sub>8</sub>)<sup>+</sup> (7) ↔ {Fe(NO)<sub>2</sub>}<sup>10</sup>-{Fe(NO)<sub>2</sub>}<sup>9</sup> 1 ↔ {Fe(NO)<sub>2</sub>}<sup>10</sup>-{Fe(NO)<sub>2</sub>}<sup>10</sup> [Fe(NO)<sub>2</sub>(μ-bdmap)Fe(NO)<sub>2</sub>]<sup>-</sup> (6) and characterize the formation of complex 1. Also, the synthesis study and DFT computation feature the detailed mechanism of electronically localized {Fe(NO)<sub>2</sub>}<sup>10</sup>-{Fe(NO)<sub>2</sub>}<sup>9</sup> DNIC 1 reducing NO to N<sub>2</sub>O via the associated hyponitrite-formation and NO-disproportionation pathways. Presumably, the THF-bound {Fe(NO)<sub>2</sub>}<sup>9</sup> unit of electronically localized {Fe(NO)<sub>2</sub>}<sup>10</sup>-{Fe(NO)<sub>2</sub>}<sup>9</sup> complex 1 served as an electron buffering reservoir for accommodating electron redistribution, and the {Fe(NO)<sub>2</sub>}<sup>10</sup> unit of complex 1 acted as an electron-transfer channel to drive exogenous ·NO coordination to yield proposed relay intermediate κ<sup>2</sup>-N,O-[NO]<sup>-</sup>-bridged [Fe<sub>2</sub>(NO)<sub>4</sub>(μ-bdmap)(μ-NO)] (A) for NO reduction to N<sub>2</sub>O.

### INTRODUCTION

Nitric oxide (·NO) was demonstrated as a versatile physiological regulator for vasodilation, immune response, and neurotransmission in mammals.<sup>1</sup> Mammals exhibit regular metabolism precisely modulating the concentration of nitric oxide to relieve nitrosative stress via the metal-mediated oxygenation of ·NO yielding nitrite/nitrate ions.<sup>1–3</sup> The mammalian immune response defends against invading pathogens by producing ·NO and its derivative in macrophages.<sup>1–3</sup> Some pathogens employ heme-/Cu-containing or heme-/nonheme-containing nitric oxide reductases (NORs),<sup>4–7</sup> flavin diiron NORs (FNORs),<sup>5,8–12</sup> and flavin-free diiron NORs (e.g., microbial YtfE repair protein)<sup>13</sup> serving as an NO trapper/scavenger to facilitate the reductive coupling of ·NO producing nitrous oxide (N<sub>2</sub>O) under the participation of electrons and protons. In the diiron NORs, the prerequisite

for N<sub>2</sub>O liberation requires the cooperative nitrosylation of diiron sites [Fe(II)–Fe(II)]. Two scenarios were proposed for ON–NO bond formation: (a) The hyponitrite pathway involving the addition of exogenous ·NO to a proposed mononitrosyl-bridged (κ<sup>2</sup>-N,O-NO) [Fe(II)–{Fe(NO)}<sup>7</sup>] species forms a putative hyponitrito-bound intermediate.<sup>14</sup> (b) Diferrous dinitrosyl pathway: ON–NO coupling occurs via the dinitrosyl diiron [{Fe(NO)}<sup>7/8</sup>-{Fe(NO)}<sup>7/8</sup>] inter-

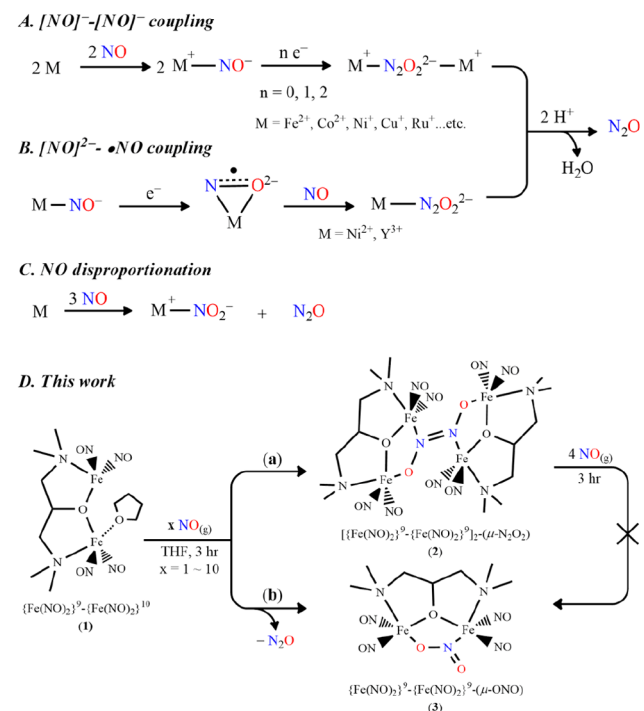
**Special Issue:** Renaissance in NO Chemistry

**Received:** February 22, 2021

mediate to release  $\text{N}_2\text{O}$ ,<sup>15,16</sup> where Enemark–Feltham notation is adopted.<sup>17</sup>

In biomimetic model studies, transition-metal-complex-mediated NO conversion to  $\text{N}_2\text{O}$  via inter/intramolecular ON–NO coupling has been explored (Scheme 1A).<sup>18–37</sup> The

### Scheme 1. NO Reduction to $\text{N}_2\text{O}$ Triggered by Transition-Metal Complexes



reductive conversion of  $\bullet\text{NO}$  to  $\text{N}_2\text{O}$  via the formation of hyponitrite-bound intermediate ( $[\text{ON}]^-$ – $[\text{NO}]^-$  coupling promoted by ligating two Fe-/Ru-nitrosyl moieties,<sup>22,29</sup> stabilized by Lewis acid<sup>31</sup> or hydrogen-bonding interactions<sup>32,33</sup>) was demonstrated. In particular, it has been reported that the highly reduced  $[\text{NO}]^{2-}$ -bound complexes possessing a stronger nucleophilicity promote  $\bullet\text{NO}$  electrophilic attack to form hyponitrite-bound complexes (Scheme 1B).<sup>33–36</sup> NO disproportionation yielding nitrite and  $\text{N}_2\text{O}$  triggered by transition-metal (Fe, Cu, Ni, Co, Ru, and Mn) complexes was also proposed (Scheme 1C).<sup>38–48</sup> Despite several literature reports on the transition-metal-mediated reduction of NO to  $\text{N}_2\text{O}$ , the detailed conversion pathways of NO to  $\text{N}_2\text{O}$  via competition between the generation of the  $[\text{N}_2\text{O}_2]^{2-}$ -bound intermediate and the formation of the  $[\text{N}_2\text{O}_2]^-$ -bound intermediate originated from metal-mediated NO disproportionation remain elusive.

The natural  $[\text{Fe}(\text{NO})_2]$  motifs in the form of dinitrosyl iron complexes (DNICs) derived from the nitrosylation of nonheme Fe proteins or the assembly of nonheme iron and endogenous  $\bullet\text{NO}$  in the presence of glutathione/cysteine/histidine were demonstrated.<sup>49–52</sup> Glutathione transferase (GST) was demonstrated to act as the storing/transporting protein of DNICs, and multi-drug-resistance-associated protein 1 was unveiled as the effluent channel of DNICs.<sup>53–57</sup> In the biomimetic study of DNICs, the redox shuttling of DNICs  $[(\text{NO})_2\text{FeL}_2]$  between  $\{\text{Fe}(\text{NO})_2\}^9$  and  $\{\text{Fe}(\text{NO})_2\}^{10}$  electronic states, modulated by the RS-/R<sub>2</sub>N-/RO-coordinate

ligands,<sup>58</sup> was reported to stabilize  $\bullet\text{NO}/\text{NO}^-$ ,<sup>58,59</sup> activate nitrite/nitrate,<sup>60,61</sup> and trigger  $\text{CO}_2$  reduction.<sup>62</sup> Because of the two spin-parallel NO ligands of DNICs, it was demonstrated that the spontaneous intramolecular ON–NO coupling of the  $[\text{Fe}(\text{NO})_2]$  unit does not occur.<sup>26,52,63</sup> In a recent communication, we reported that electronically localized dinuclear  $\{\text{Fe}(\text{NO})_2\}^{10}$ – $\{\text{Fe}(\text{NO})_2\}^9$  DNIC  $[\text{Fe}(\text{NO})_2(\mu\text{-bdmap})\text{Fe}(\text{NO})_2(\text{THF})]$  (**1**) (bdmap = 1,3-bis(dimethylamino)-2-propanolate) drives 1 equiv of NO reduction to yield  $\text{N}_2\text{O}$  in the presence of H-bdmap in THF via the formation of hyponitrite-bound  $\{[\text{Fe}_2(\text{NO})_4(\mu\text{-bdmap})]_2(\kappa^4\text{-N}_2\text{O}_2)\}$  (**2**) (yield  $\sim 74\%$ ).<sup>28b</sup> In this study, we uncover that the NO-to- $\text{N}_2\text{O}$  transformation triggered by dinuclear **1** in the presence of various amounts of exogenous  $\bullet\text{NO}$  occurs via the simultaneous formation of hyponitrite-bound intermediate **2** (by adopting the intermolecular  $[\text{ON}]^-$ – $[\text{NO}]^-$  coupling pathway) and  $[\text{NO}_2]^-$ -bridged  $[\text{Fe}_2(\text{NO})_4(\mu\text{-bdmap})(\mu\text{-NO}_2)]$  (**3**) along with the release of  $\text{N}_2\text{O}$  (by adopting the NO disproportionation pathway) (Scheme 1D). In addition, the revealed synthesis cycle, complex **1**  $\rightarrow$   $[\text{Fe}(\text{NO})_2(\mu\text{-bdmap})(\mu\text{-NO})\text{Fe}(\text{NO})_2]$  (**A**)  $\rightarrow$  complex **3**  $\rightarrow$   $[\text{Fe}_2(\text{NO})_4(\mu\text{-bdmap})(\mu\text{-OMe})]$  (**4**)  $\rightarrow$   $[\text{Fe}_2(\text{NO})_4(\mu\text{-bdmap})(\mu\text{-OSO}_2\text{CF}_3)]$  (**5**)  $\rightarrow$  complex **1** (as shown in Scheme 2), highlights the proposed ( $\kappa^2$ - $[\text{NO}]^-$ )-bridged dinuclear  $\{\text{Fe}(\text{NO})_2\}^9$ – $\{\text{Fe}(\text{NO})_2\}^9$   $[\text{Fe}(\text{NO})_2(\mu\text{-bdmap})(\mu\text{-NO})\text{Fe}(\text{NO})_2]$  (**A**) serving as a key species for dinuclear DNIC **1**-mediated NO reduction generating  $\text{N}_2\text{O}$  via both the hyponitrite-formation pathway and the NO disproportionation pathway (Scheme 2b,c).

## RESULTS AND DISCUSSION

As displayed in Figure 1, the addition of 1 equiv of NO to the THF solution of complex  $[\text{Fe}(\text{NO})_2(\mu\text{-bdmap})\text{Fe}(\text{NO})_2(\text{THF})]$  (**1**) yielded the major product of complex  $\{[\text{Fe}_2(\text{NO})_4(\mu\text{-bdmap})]_2(\kappa^4\text{-N}_2\text{O}_2)\}$  (**2**) (1741 sh ( $\nu_{\text{NO}}$ ), 1719 m, 1667 sh, and 1651 m  $\text{cm}^{-1}$ ; yield  $71.8 \pm 7.7\%$ ) and the minor product  $[\text{Fe}_2(\text{NO})_4(\mu\text{-bdmap})(\mu\text{-NO}_2)]$  (**3**) (1759 s and 1693 s  $\text{cm}^{-1}$  ( $\nu_{\text{NO}}$ ), yield  $\sim 25.4 \pm 6.9\%$ ) along with the release of  $\text{N}_2\text{O}$  ( $\sim 2223 \text{ cm}^{-1}$  ( $\nu_{\text{N-N}}$ ), yield  $\sim 23.2 \pm 3.54\%$ ).<sup>28b</sup> In contrast, the reaction of complex **1** with 3 equiv of NO(g) in THF (2 mL) at ambient temperature for 3 h led to the formation of suspended powder **2** (yield  $\sim 19.3 \pm 8.7\%$ ) and the brown solution of complex **3** (yield  $\sim 76.2 \pm 10.2\%$ ) along with release of  $\text{N}_2\text{O}$  (yield  $\sim 75.8 \pm 11.8\%$ ) characterized by GC (Figure 1, Figures S1 and S2, and Scheme 2a–c). In a similar fashion, the treatment of 2 equiv of NO(g) with complex **1** in THF yielded complex **2**, complex **3**, and  $\text{N}_2\text{O}$  in yields of  $47.0 \pm 9.1$ ,  $48.6 \pm 9.7$ , and  $\sim 46.7 \pm 9.0\%$  (Figure 1b). It is noted that the reaction of complex **1** with greater amounts of NO(g) ( $>3$  equiv of NO) does not significantly change the yield distribution of complex **2** (yield 10–15%), complex **3** (yield 75–85%), and  $\text{N}_2\text{O}$  (yield 75–88%) (Figure 1). Of importance, complex **2** did not transform to complex **3** when 4 equiv of NO was added to the THF solution of complex **2** and stirred for 3 h at ambient temperature (Figure S3). These results suggest that the simultaneous generation of complexes **2** and **3** and  $\text{N}_2\text{O}$  may be derived from the distinct pathways when NO(g) is added to the THF solution of complex **1** at ambient temperature. Specifically, the simultaneous production of complexes **2** and **3** and  $\text{N}_2\text{O}$  may occur via the intermolecular  $[\text{ON}]^-$ – $[\text{NO}]^-$  coupling of the proposed  $\{\text{Fe}(\text{NO})_2\}^9$ – $\{\text{Fe}(\text{NO})_2\}^9$   $\kappa^2$ - $[\text{NO}]^-$ -bridged  $[\text{Fe}_2(\text{NO})_4(\mu\text{-bdmap})(\mu\text{-NO})]$  (**A**) (hyponitrite-formation pathway

**Scheme 2. Synthesis Cycles for the Hyponitrite-Formation Pathway (1 → 2 → 5 → 1) and NO Disproportionation Pathway (1 → 3 → 4 → 5 → 1) Triggered by Complex 1 via Relay Intermediate A**

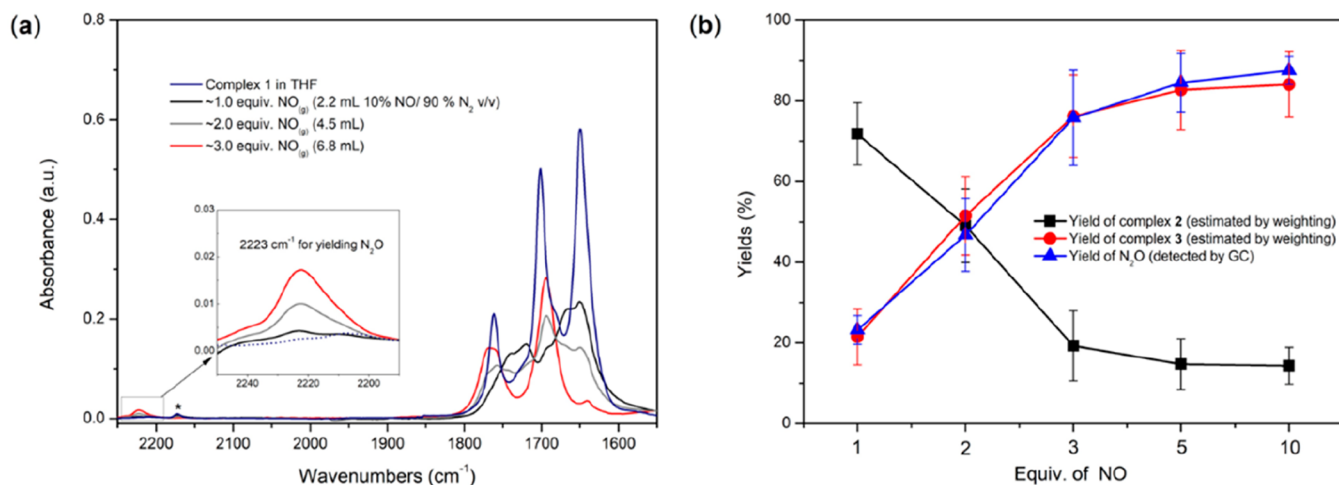
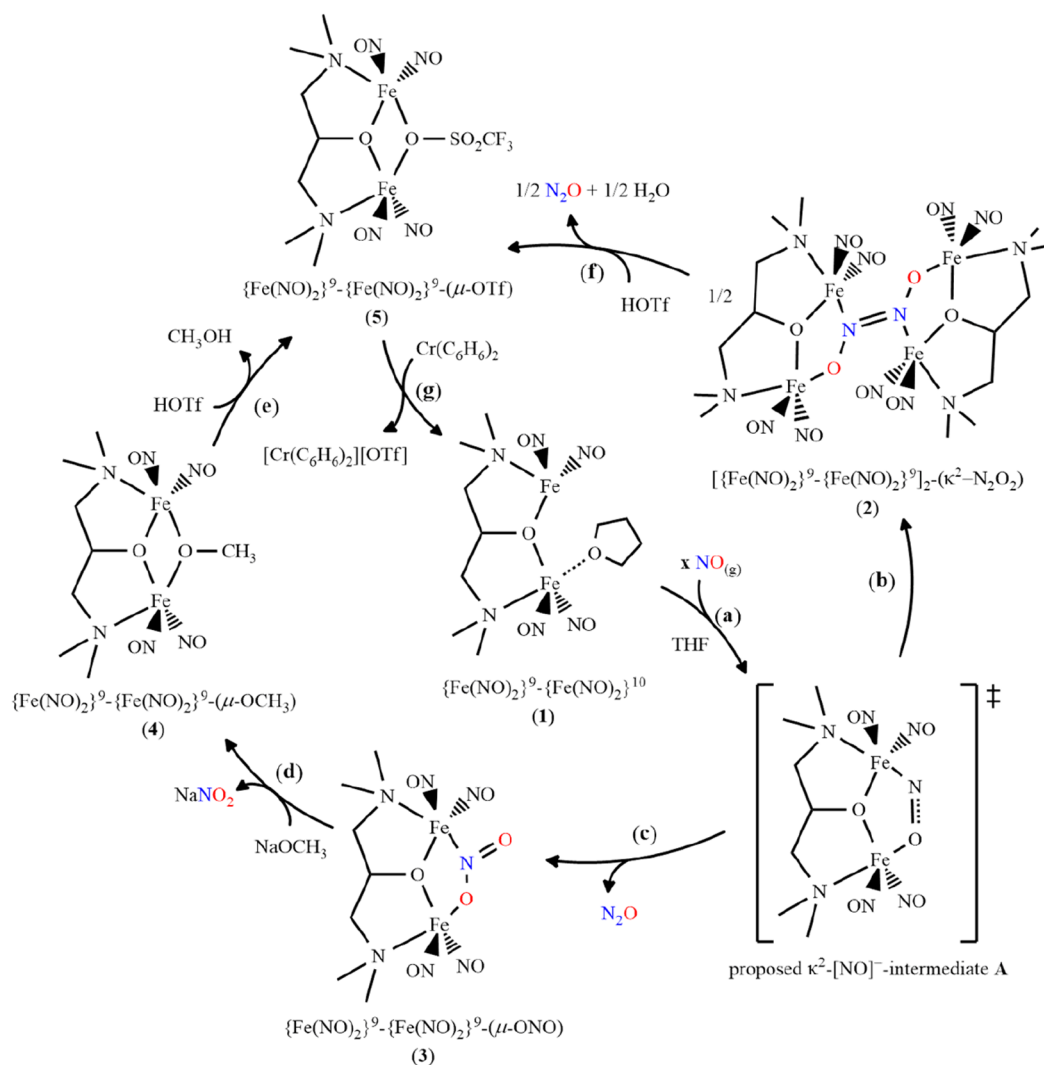


**Figure 1.** (a) FTIR spectra of complex 1 reacted with various equiv of NO(g) in THF, in which \* is an undefined impurity. (b) Yield of complexes 2 (black line) and 3 (red line) along with N<sub>2</sub>O (blue line) for the reaction of various quantities of NO(g) with 1. (Also see Figures S1 and S2.)

(Scheme 2b)) accompanied by the electrophilic attack of NO on relay intermediate A (NO disproportionation pathway

(Scheme 2c)). That is, proposed intermediate A may play a unique role in modulating NO transformation to N<sub>2</sub>O via a

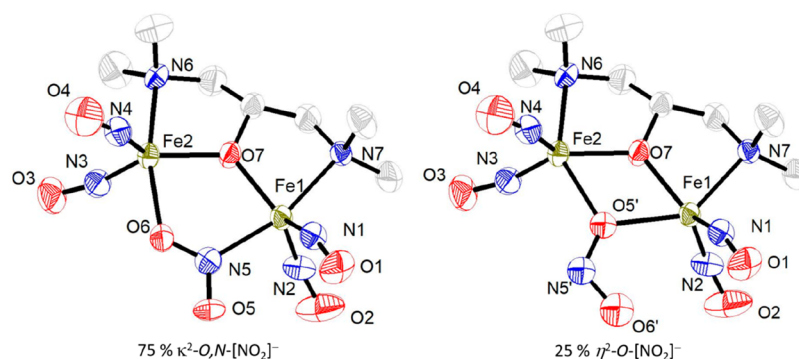


**Figure 2.** ORTEP drawing and labeling scheme of  $\{[\text{Fe}(\text{NO})_2]_2(\mu\text{-bdmap})(\mu\text{-NO}_2)\}$  with the thermal ellipsoid drawn at 50% probability (the ratio of  $\kappa^2\text{-O,N-}[\text{NO}_2]^-$   $\{[\text{Fe}(\text{NO})_2]_2(\mu\text{-bdmap})(\mu\text{-NO}_2)\}$  (3) and  $\eta^2\text{-O-}[\text{NO}_2]^-$   $\{[\text{Fe}(\text{NO})_2]_2(\mu\text{-bdmap})(\mu\text{-NO}_2)\}$  (3') = 0.75:0.25). Hydrogen atoms are omitted for clarity. Selected bond lengths (Å) and angles (deg) are presented in Table S1.

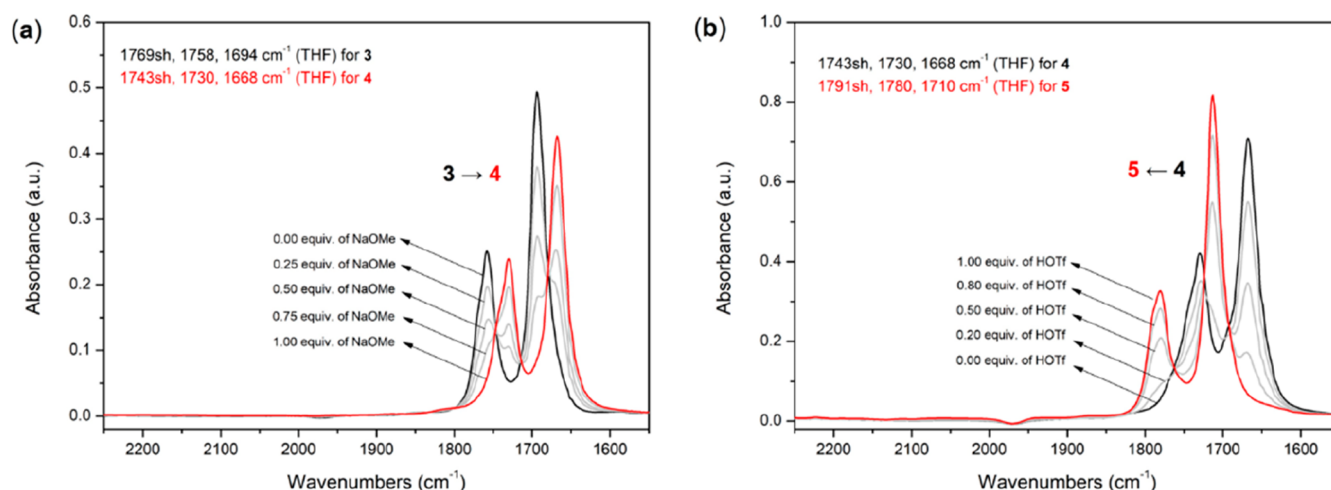


**Figure 3.** (a) FTIR spectra for the addition of 0.0–1.0 equiv of  $\text{NaOCH}_3$  to complex 3 (black line), yielding complex 4 (red line) in THF. (b) FTIR spectra for the addition of 0.0–1.0 equiv of HOTf to complex 4 (black line), yielding complex 5 (red line) in THF at  $-80^\circ\text{C}$ .

associated hyponitrite-formation pathway (intermolecular  $[\text{ON}]^-$ – $[\text{NO}]^-$  coupling) and NO disproportionation pathway (Scheme 2b,c). Attempts to detect intermediate A were unsuccessful when complex 1 was reacted with excess NO in THF by low-temperature UV–vis/FTIR spectroscopy ( $-80^\circ\text{C}$ ) (Figure S4). Theoretical calculations of Gibbs free-energy profiles of the reaction mechanism as well as the analysis of natural charge and spin density distributions were then conducted to elaborate how key intermediate A dictates NO reduction to  $\text{N}_2\text{O}$  via the associated pathways of  $[\text{ON}]^-$ – $[\text{NO}]^-$  coupling and NO disproportionation, as shown in the Computation section.

The crystallographic structure of complex 3 is depicted in Figure 2, and the selected bond distances and angles are presented in Table S1. The bond lengths of Fe–N(O) range from 1.681(5) to 1.703(5) Å, and the N–O bond lengths are within 1.154(6)–1.174(6) Å, consistent with the published Fe–N(O) and N–O bond lengths of  $\{\text{Fe}(\text{NO})_2\}^9$  DNICs.<sup>58–76</sup> It is noticed that complex 3 shows linkage isomers, that is, complex 3 with  $\kappa^2\text{-O,N-NO}_2$  linkage (O(5)–N(5)–O(6) (75%)) and complex 3' with terminal  $\eta^2\text{-O-ONO}$  linkage (O(5')–N(5')–O(6')) (25%). Variable-temperature UV–vis spectra indicate that the linkage isomers of complex 3 with  $\kappa^2\text{-O,N-NO}_2$  and complex 3' with  $\eta^2\text{-O-ONO}$  are interconvertible, as shown in Figure S5. The Fe(1)⋯Fe(2) distance of 3.543 Å found in  $\{\text{Fe}(\text{NO})_2\}^9$ – $\{\text{Fe}(\text{NO})_2\}^9$

complex 3 rationalizes the less dipolar interaction reflecting the paramagnetic property. The EPR spectrum (solid) of complex 3 shows an isotropic signal at  $g = 2.020$  corresponding to a paramagnetic species (Figure S6). The temperature-dependent effective magnetic moment of complex 3 ranging from  $2.75\mu_{\text{B}}$  (300 K) to  $0.53\mu_{\text{B}}$  (2 K) and the best-fit  $\chi_{\text{M}}T$  value (versus absolute temperature for  $g = 2.030$ ,  $J = -45.3 \pm 0.5 \text{ cm}^{-1}$ ) demonstrate the antiferromagnetic coupling between two  $\{\text{Fe}(\text{NO})_2\}^9$  ( $S = 1/2$ ) units (Figures S7 and S8). Also, the Fe K-edge pre-edge energy of 7113.8 eV suggests the  $\{\text{Fe}(\text{NO})_2\}^9$ – $\{\text{Fe}(\text{NO})_2\}^9$  electron configuration of complex 3 (Figure S9).<sup>58,75,76</sup>

In contrast to the injection of NO(g) into the fully delocalized mixed-valence  $\{\text{Fe}(\text{NO})_2\}^{10}$ – $\{\text{Fe}(\text{NO})_2\}^9$   $[\text{Fe}_2(\mu\text{-S}^t\text{Bu})_2(\text{NO})_4]^-$  (EPR signal  $g_{\perp} = 2.009$  and  $g_{\parallel} = 1.965$  at 77 K and IR  $\nu_{\text{NO}}$  1673 s, 1655 s (THF)) yielding  $\{\text{Fe}(\text{NO})_2\}^9$ – $\{\text{Fe}(\text{NO})_2\}^9$   $[\text{Fe}_2(\mu\text{-S}^t\text{Bu})_2(\text{NO})_4]$ ,<sup>68</sup> the addition of NO gas to the THF solution of complex 1 leading to the formation of complexes 2 and 3 and  $\text{N}_2\text{O}$  suggests that electronically localized  $\{\text{Fe}(\text{NO})_2\}^{10}$ – $\{\text{Fe}(\text{NO})_2\}^9$  DNIC 1 acts as a key species in promoting the electrophilic attack of NO on the  $\{\text{Fe}(\text{NO})_2\}^{10}$  core of complex 1, yielding proposed  $\kappa^2$ -[NO]<sup>−</sup>-bridged intermediate A. The electrochemistry of complex 3 measured in THF with 0.1 M  $[n\text{-Bu}_4\text{N}][\text{PF}_6]$  as supporting electrolyte at room temperature displaying irreversible redox signals at  $E_{\text{pc}} = -1.25$  and  $-1.96$  V and  $E_{\text{pa}} = -0.86$  V (vs Fc/

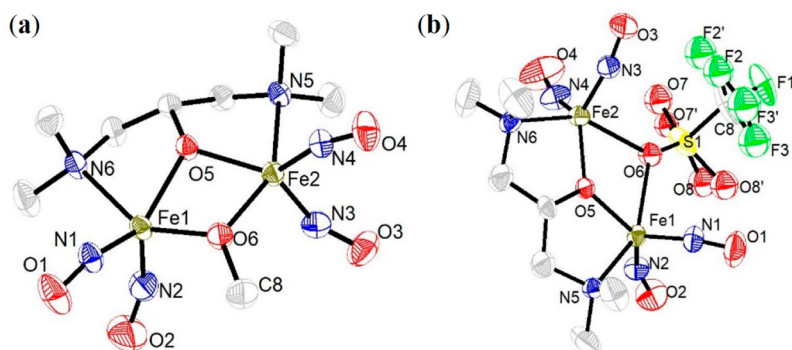


**Figure 4.** ORTEP drawing and labeling schemes of (a) complex 4 and (b) complex 5 with the thermal ellipsoid drawn at 50% probability. Hydrogen atoms are omitted for clarity. Selected bond lengths (Å) and angles (deg) are presented in Table S1.

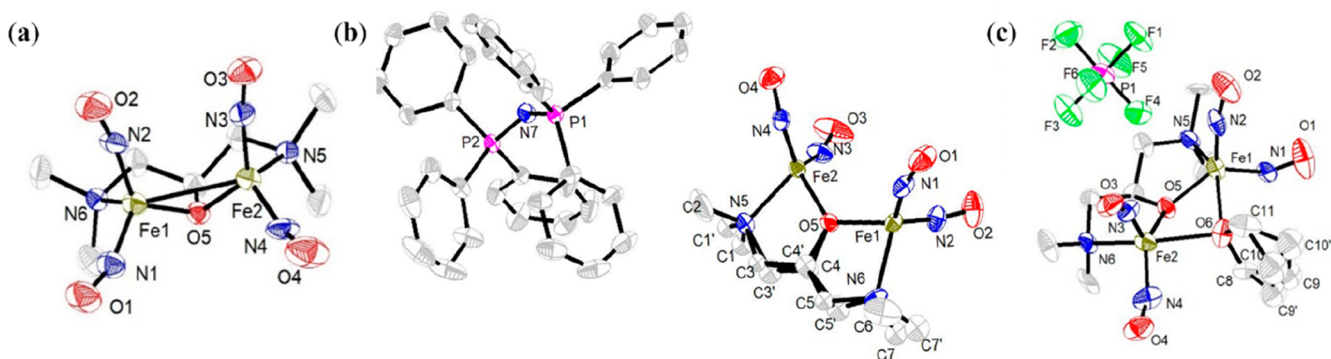


**Figure 5.** ORTEP drawing and labeling schemes of (a) complex 1', (b) complex 6, and (c) complex 7 with the thermal ellipsoid drawn at 50% probability. Hydrogen atoms are omitted for clarity. Selected bond lengths (Å) and angles (deg) are presented in Table S1.

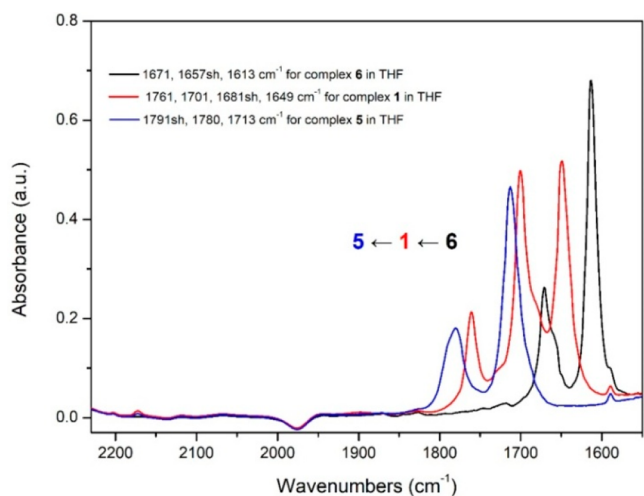
$\text{Fc}^+$ ) implies that the direct reduction of complex 3 to complex 1 to complete the catalytic cycle of NO to  $\text{N}_2\text{O}$  is infeasible (Figure S10). Alternatively, the transformation of complex 3 to  $[\text{Fe}_2(\text{NO})_4(\mu\text{-bdmap})(\mu\text{-OMe})]$  (4) along with release of  $\text{NaNO}_2$  was observed upon addition of 1 equiv of  $[\text{Na}][\text{OCH}_3]$  to complex 3 in THF at ambient temperature. The lower NO stretching frequencies of complex 4 (1743 sh, 1730 s, 1668  $\text{s cm}^{-1}$  ( $\nu_{\text{NO}}$ )), compared to those of complex 3 (1759 s, 1693  $\text{s cm}^{-1}$  ( $\nu_{\text{NO}}$ )), suggest the electronic deficiency of the dinuclear  $\{\text{Fe}(\text{NO})_2\}^9\text{-}\{\text{Fe}(\text{NO})_2\}^9$   $[(\text{NO})_2\text{Fe}(\mu\text{-bdmap})\text{Fe}(\text{NO})_2]$  motif (Scheme 2d and Figure 3a). The yield of  $\text{NaNO}_2$  was extracted by  $\text{O}_2$ -free water and was quantified via Griess assay (72.4% yield, Figure S11). The electrochemistry of complex 4 measured in THF with 0.1 M  $[n\text{-Bu}_4\text{N}][\text{PF}_6]$  as the supporting electrolyte at room temperature displaying irreversible redox signals at  $E_{\text{pc}} = -1.86$  V and  $E_{\text{pa}} = -1.04$  V (decayed to  $E_{\text{pa}} = -0.95$  V in the second cycle (vs  $\text{Fc}/\text{Fc}^+$ )) demonstrates that complex 4 undergoes decomposition when complex 4 is reduced to  $\{\text{Fe}(\text{NO})_2\}^9\text{-}\{\text{Fe}(\text{NO})_2\}^{10}$  DNIC (Figure S12). To complete the synthesis cycle for reducing nitric oxide to  $\text{N}_2\text{O}$  triggered by complex 1, the protonation of complex 4 by triflic acid was conducted to result in the formation of redox-reversible  $\{\text{Fe}(\text{NO})_2\}^9\text{-}\{\text{Fe}(\text{NO})_2\}^9$  triflate-bridged  $[\text{Fe}_2(\text{NO})_4(\mu\text{-bdmap})(\mu\text{-OSO}_2\text{CF}_3)]$  (5) (1791 sh, 1780 s, 1710  $\text{s cm}^{-1}$  ( $\nu_{\text{NO}}$ )) and MeOH at  $-80$  °C (Scheme 2e and Figure 3b). Similarly, the formation of complex 5 along with  $\text{N}_2\text{O}$  liberation was also observed by the protonation (triflic acid) of hyponitrite-bound complex 2 at 0 °C (Scheme 2f and Figure S13). Subsequently, the addition of 1 equiv of bis(benzene)chromium ( $\text{CrBz}_2$ ) to the THF solution of complex 5 generated complex 1 to complete the

synthesis cycle for reducing NO to  $\text{N}_2\text{O}$  triggered by complex 1 via the associated pathways of hyponitrite formation (synthesis cycle complex 1  $\rightarrow$  2  $\rightarrow$  5  $\rightarrow$  1) and NO disproportionation (synthesis cycle complex 1  $\rightarrow$  3  $\rightarrow$  4  $\rightarrow$  5  $\rightarrow$  1) (Scheme 2 and Figure S14).

The crystallographic structures of complexes 4 and 5 are depicted in Figure 4, and the selected bond distances and angles are presented in Table S1. The average Fe–N(O)/N–O bond lengths of methoxide-bridged complex 4 and triflate-bridged complex 5 are 1.702(5)/1.175(3) Å (for 4) and 1.692(5)/1.164(6) Å (for 5), respectively, characterized as dinuclear  $\{\text{Fe}(\text{NO})_2\}^9\text{-}\{\text{Fe}(\text{NO})_2\}^9$  DNICs.<sup>58–76</sup> Presumably, the elongation of N–O bond lengths of complex 4 (ranging from 1.170(3) to 1.183(3) Å), compared to those of complex 5 (ranging from 1.159(7) to 1.169(6) Å), reflects the methoxide-induced polarization of five-coordinate iron centers leading to the  $[\text{Fe}^{3+}(\text{NO}^-)_2]$  units to preserve the highly covalent  $\{\text{Fe}(\text{NO})_2\}^9$  cores.<sup>76</sup> EPR spectra of complexes 4 and 5 (solid) exhibit an isotropic signal at  $g = 2.036$  and a broad isotropic signal at  $g = 2.034$ , respectively, corresponding to the paramagnetic species (Figures S15 and S16). The temperature-dependent effective magnetic moment of complex 4 (from  $2.23\mu_{\text{B}}$  (300 K) to  $0.89\mu_{\text{B}}$  (2 K)) and complex 5 (from  $2.72\mu_{\text{B}}$  (300 K) to  $0.78\mu_{\text{B}}$  (2 K)) and the corresponding best-fit  $\chi_{\text{M}}T$  values for complexes 4 ( $g = 2.035$ ,  $J = -172.57 \pm 4.87$   $\text{cm}^{-1}$ ) and 5 ( $g = 2.030$ ,  $J = -111.1 \pm 1.7$   $\text{cm}^{-1}$ ) indicate the antiferromagnetically coupling between two  $\{\text{Fe}(\text{NO})_2\}^9$  ( $S = 1/2$ ) cores (Figures S7, S17, and S18). The Fe K-edge pre-edge energies of complex 4 (7114.0 eV) and complex 5 (7114.0 eV) also suggest the  $\{\text{Fe}(\text{NO})_2\}^9\text{-}\{\text{Fe}(\text{NO})_2\}^9$

electron configuration for complexes **4** and **5** (Figure S9).<sup>58,75,76</sup>

To further unravel the exact electron configuration of two  $[\text{Fe}(\text{NO})_2]$  units of  $\{\text{Fe}(\text{NO})_2\}^{10}-\{\text{Fe}(\text{NO})_2\}^9$  dinuclear DNIC **1**, the deep-blue THF solution of complex **1** layered with *n*-hexane (10 mL) was kept at  $-20^\circ\text{C}$  for 1 week leading to dark-green crystals of  $[\text{Fe}(\text{NO})_2(\mu\text{-bdmap})\text{Fe}(\text{NO})_2]$  (**1'**) composed of two four-coordinate iron centers. The single-crystal X-ray structure of complex **1'** is depicted in Figure S5a, and the selected bond distances and angles are shown in Table S1. The bond lengths of Fe–N(O) range from 1.649(5) to 1.657(5) Å and the N–O bond lengths range from 1.179(6) to 1.192(6) Å, compared to the published Fe–N(O) (1.661(2) Å) and N–O (1.186(2) Å) bond lengths of  $\{\text{Fe}(\text{NO})_2\}^9-\{\text{Fe}(\text{NO})_2\}^{10}$  DNICs,<sup>68,73</sup> supporting the crystallization of the singly bdmap-bridged electronically delocalized  $\{\text{Fe}(\text{NO})_2\}^9-\{\text{Fe}(\text{NO})_2\}^{10}$  solid-state  $[\text{Fe}(\text{NO})_2(\mu\text{-bdmap})\text{Fe}(\text{NO})_2]$  (**1'**). We noticed the absence of the THF-coordinate ligand in isolated solid-state crystal DNIC **1'**. It is presumed that the thermal stability of solid-state  $\{\text{Fe}(\text{NO})_2\}^9-\{\text{Fe}(\text{NO})_2\}^{10}$  DNIC **1'** may be ascribed to the apparently shorter Fe··Fe distance (2.806(1) Å) to reimburse the electronic deficiency of  $[\text{Fe}(\text{NO})_2]$  cores. However, the single-crystal X-ray structure of DNIC **1'**, obtained from the deep-blue THF solution of complex **1** layered with *n*-hexane and kept at  $-20^\circ\text{C}$  for 1 week, was analyzed as dark-green  $[\text{Fe}(\text{NO})_2(\mu\text{-bdmap})\text{Fe}(\text{NO})_2]$  (**1'**). Dark-green crystal DNIC **1'** dissolved in THF to yield the IR spectrum ( $\nu_{\text{NO}}$  1762 m, 1701 s, 1682 sh, 1650  $\text{cm}^{-1}$  (THF)), suggesting the formation of complex **1**. Further addition of 1 equiv of  $\text{KC}_8 + [\text{PPN}][\text{Cl}]$  to a THF solution of complex **1'** afforded the reduced-form dinuclear  $\{\text{Fe}(\text{NO})_2\}^{10}-\{\text{Fe}(\text{NO})_2\}^{10}$  DNIC  $[\text{PPN}][\text{Fe}(\text{NO})_2(\mu\text{-bdmap})\text{Fe}(\text{NO})_2]$  (**6**) verified by IR (1671 s, 1657 sh, 1613  $\text{cm}^{-1}$  ( $\nu_{\text{NO}}$ )) and single-crystal X-ray diffraction (Figures S5b and 6

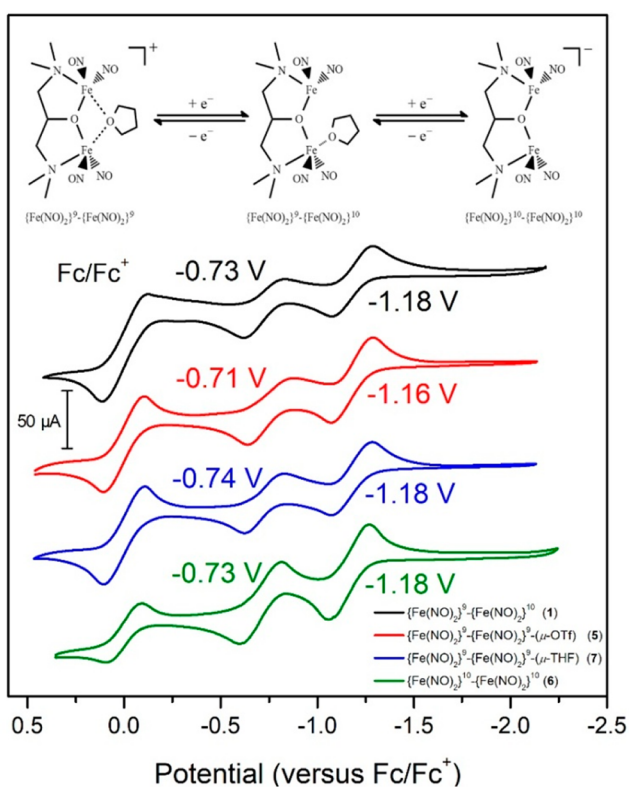
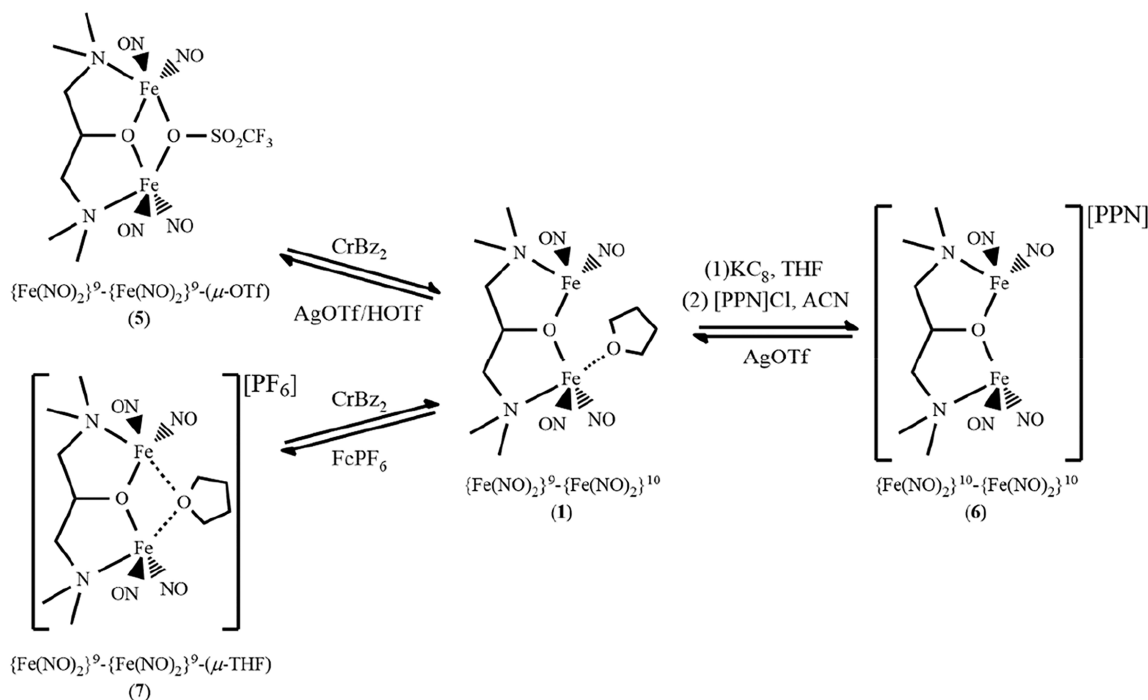


**Figure 6.** FTIR spectra for the addition of 1 and 2 equiv of silver triflate to complex **6** (black) in THF, yielding complex **1** (red) and complex **5** (blue), respectively.

and Scheme 3). Of importance, the electrochemistry of complex **6** measured in THF with 0.1 M  $[n\text{-Bu}_4\text{N}][\text{PF}_6]$  as the supporting electrolyte at room temperature reveals two reversible redox processes at  $E_{1/2} = -0.71$  V ( $\Delta E_p = 0.21$  V,  $i_{pa}/i_{pc} = 1.03$ ) and  $-1.16$  V ( $\Delta E_p = 0.21$  V,  $i_{pa}/i_{pc} = 0.93$  vs  $\text{Fc}/\text{Fc}^+$ ), exactly consistent with the cyclic voltammetric study of complex **1** displaying two reversible redox couples ( $E_{1/2}$ ) at

$-0.73$  and  $-1.18$  V (vs  $\text{Fc}/\text{Fc}^+$ ) (Figure 7). That is, the redox-form DNICs associated with  $\{\text{Fe}(\text{NO})_2\}^9-\{\text{Fe}(\text{NO})_2\}^9$  DNIC  $\leftrightarrow \{\text{Fe}(\text{NO})_2\}^{10}-\{\text{Fe}(\text{NO})_2\}^9$  DNIC **1**  $\leftrightarrow \{\text{Fe}(\text{NO})_2\}^{10}-\{\text{Fe}(\text{NO})_2\}^{10}$  DNIC **6** electronic states are reversible (Scheme 3 and Figure 7). This result obtained from the cyclic voltammetric study is supported by the treatment of the THF solution of complex **1** with ferrocenium hexafluorophosphate ( $\text{FcPF}_6$ ), yielding oxidized-form dinuclear  $\{\text{Fe}(\text{NO})_2\}^9-\{\text{Fe}(\text{NO})_2\}^9$   $[\text{Fe}_2(\text{NO})_4(\mu\text{-bdmap})(\mu\text{-THF})][\text{PF}_6]$  (**7**) with the THF-bridged ligand (Scheme 3), characterized by IR (1790 sh, 1776 s, 1710  $\text{cm}^{-1}$  ( $\nu_{\text{NO}}$ )) and single-crystal X-ray diffraction (Figure 5c and S19). In a similar fashion, the addition of 1 equiv of silver triflate ( $\text{AgOTf}$ ) to complex **6** in THF led to the formation of complex **1**, and the subsequent addition of 1 equiv of  $\text{AgOTf}$  to complex **1** resulted in the isolation of  $\{\text{Fe}(\text{NO})_2\}^9-\{\text{Fe}(\text{NO})_2\}^9$   $[\text{Fe}_2(\text{NO})_4(\mu\text{-bdmap})(\mu\text{-OSO}_2\text{CF}_3)]$  (**5**) as identified by IR (1790 sh, 1776 s, 1710  $\text{cm}^{-1}$  ( $\nu_{\text{NO}}$ )) and single-crystal X-ray diffraction (Scheme 3, Figures 5–6). Presumably, the redox-inactive  $\mu\text{-SO}_2\text{CF}_3/\text{THF}$ -bridging ligands of complexes **5/7**, individually, are incorporated to stabilize the highly covalent dinuclear  $\{\text{Fe}(\text{NO})_2\}^9-\{\text{Fe}(\text{NO})_2\}^9$   $[\text{Fe}_2(\text{NO})_4(\mu\text{-bdmap})]$  motif via its ability to donate electron density. Consistent with the previous cyclic voltammetric study of complexes **1/6** displaying two reversible redox couples, complexes **5** and **7** exhibit two identical redox couples at  $E_{1/2} = -0.74$  and  $-1.18$  V for **5** and at  $E_{1/2} = -0.73$  and  $-1.18$  V for **7**, respectively (Figure 7). The electrochemical/chemical studies of  $\{\text{Fe}(\text{NO})_2\}^9-\{\text{Fe}(\text{NO})_2\}^{10}$  dark-green crystal DNIC **1'** dissolved in THF display the reversible redox interconversion among  $\{\text{Fe}(\text{NO})_2\}^9-\{\text{Fe}(\text{NO})_2\}^9$  **7**,  $\{\text{Fe}(\text{NO})_2\}^{10}-\{\text{Fe}(\text{NO})_2\}^9$  DNIC **1**, and  $\{\text{Fe}(\text{NO})_2\}^{10}-\{\text{Fe}(\text{NO})_2\}^{10}$  DNIC **6**, identifying the presence of the THF-bound ligand to stabilize the electron-deficient  $\{\text{Fe}(\text{NO})_2\}^9$  core. Also, the EPR spectrum of DNIC **1** ( $g_{\text{iso}} = 2.013$  (THF, 77 K)), consistent with the reported five-/six-coordinate  $\{\text{Fe}(\text{NO})_2\}^9$  DNICs ( $g \approx 2.01-2.02$ ), implicates the preservation of a five-coordinate  $\{\text{Fe}(\text{NO})_2\}^9$  core ( $S = 1/2$ ) in DNIC **1**.<sup>70</sup> Furthermore, it has been demonstrated that the coordination of a “hard” RO-containing ligand ( $\text{R} = \text{alkyl}$ ) polarizes the  $\{\text{Fe}(\text{NO})_2\}^9$  core to possess the dominant ionic character of  $(\text{NO})_2\text{Fe-OR}$  bonds, leading to the electron deficiency of the iron center. That is, the coordination of  $[\text{OR}]^-$  ligands (vs  $[\text{SR}]^-$ ) inducing the electron-deficient  $\{\text{Fe}(\text{NO})_2\}^9$  core is attributed to the tendency to decrease the covalent character of Fe–OR bonds. The cooperative nature of  $\text{RO} \rightarrow \text{Fe}$  and  $\text{NO} \rightarrow \text{Fe}$  charge transfers characterizes the noninnocent character of NO ligands serving as an electron buffer to attenuate the RO-induced polarization imposed on the Fe center and to preserve the highly covalent  $\{\text{Fe}(\text{NO})_2\}^9$  core.<sup>76</sup> This may rationalize the polarization effect of the Fe– $\text{O}_{\text{bdmap}}$  bond of DNIC **1**, leading to the buildup of electronically localized  $\{\text{Fe}(\text{NO})_2\}^9-\{\text{Fe}(\text{NO})_2\}^{10}$  cores within dinuclear  $\{\text{Fe}(\text{NO})_2\}^{10}-\{\text{Fe}(\text{NO})_2\}^9$  DNIC **1**. As displayed in Scheme 3, the present study in combination with the previous IR/EPR spectra of complex **1** rationalizes that electronically localized  $\{\text{Fe}(\text{NO})_2\}^9-\{\text{Fe}(\text{NO})_2\}^{10}$  dinuclear DNIC **1** may undergo reversible redox shuttling between  $\{\text{Fe}(\text{NO})_2\}^{10}-\{\text{Fe}(\text{NO})_2\}^9$  DNIC **1** and  $\{\text{Fe}(\text{NO})_2\}^9-\{\text{Fe}(\text{NO})_2\}^9$  DNIC **7** to trigger the NO reduction to  $\text{N}_2\text{O}$ .

Single-crystal X-ray structures of complexes **6** and **7** are depicted in Figure 5b,c, and the selected bond distances and angles are presented in Table S1. The bond lengths of Fe–N(O) and N–O of complex **6**, ranging from 1.645(2) to

Scheme 3. Redox Shuttling among Complexes 5/7  $\leftrightarrow$  1  $\leftrightarrow$  6

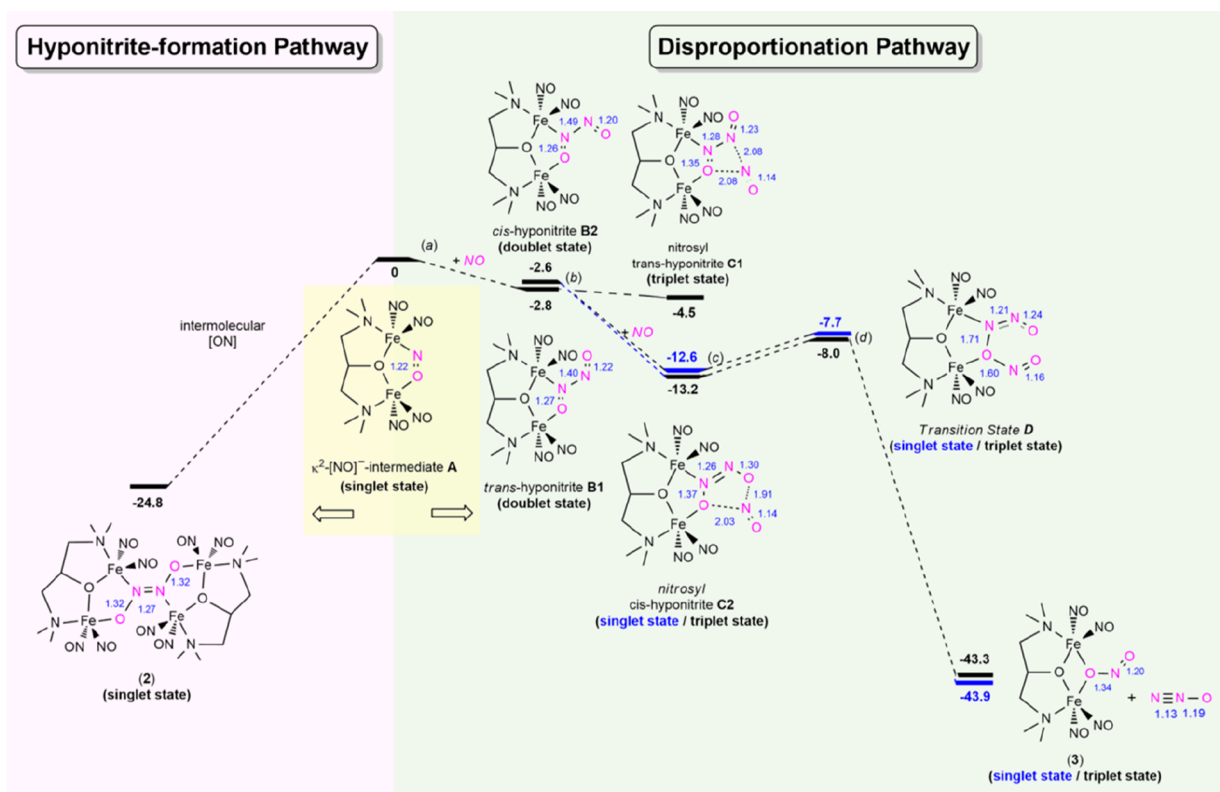
**Figure 7.** Electrochemistry of complex 1 (black), complex 5 (red), complex 6 (green), and complex 7 (blue) measured in a THF solution of complexes 1 and 5–7 (4 mM), with 0.2 M  $[n\text{-Bu}_4\text{N}][\text{PF}_6]$  as the supporting electrolyte (4 mM, ferrocene as the internal standard) at room temperature (scan rate 0.02 V/s).

1.650(2) Å and from 1.204(3) to 1.212(3) Å, respectively, are consistent with the published Fe–N(O) and N–O bond lengths of  $\{\text{Fe}(\text{NO})_2\}^{10}$  DNICs.<sup>73–75</sup> The  $^1\text{H}$  NMR spectrum

of complex 6 revealed a diamagnetic species (Figure S20). The average Fe–N(O)/N–O bond lengths of complex 7 are 1.685(2) Å/1.177(2) Å, consistent with the published Fe–N(O) and N–O bond lengths of  $\{\text{Fe}(\text{NO})_2\}^9$  DNICs.<sup>58–76</sup> The average Fe–O<sub>THF</sub> bond distance of 2.434(2) Å and the space-filling model suggest that THF bridges two  $[\text{Fe}(\text{NO})_2]$  units (Figure S21). It is presumed that the inlay of the THF ligand elongates the Fe(1)⋯Fe(2) distance (3.407(2) Å) of complex 7, leading to the weak dipolar interaction, supported by the EPR spectrum (solid) of complex 7 showing an isotropic signal at  $g = 2.037$  (Figure S22). The temperature-dependent effective magnetic moment of complex 7 (from  $2.73\mu_{\text{B}}$  (300 K) to  $0.86\mu_{\text{B}}$  (2 K)) and the corresponding best-fit  $\chi_{\text{M}}T$  value ( $g = 2.030$ ,  $J = -122.2 \pm 2.4 \text{ cm}^{-1}$ ) demonstrate the weak antiferromagnetic coupling between two  $\{\text{Fe}(\text{NO})_2\}^9$  ( $S = 1/2$ ) cores (Figures S6 and S23). The Fe K-edge pre-edge energy of 7114.0 eV in complex 7 also suggests the  $\{\text{Fe}(\text{NO})_2\}^9\text{-}\{\text{Fe}(\text{NO})_2\}^9$  electron configuration of complex 7 (Figure S9).

**Computation.** The DFT calculations of geometry-optimized  $[\text{Fe}(\text{NO})_2(\mu\text{-bdmap})\text{Fe}(\text{NO})_2]$  (1') and  $[\text{Fe}(\text{NO})_2(\mu\text{-bdmap})\text{Fe}(\text{NO})_2(\text{THF})]$  (1) were conducted, and their selected bond distances, spin densities, and natural charges are included in Figure S24a. As shown in Figure S24a, the calculated Fe–N(O)/N–O bond lengths between two  $\text{Fe}(\text{NO})_2$  fragments in complex 1' are almost equivalent, consistent with its solid-state structure determined by single-crystal X-ray diffraction. In addition, the spin density distribution of two  $\text{Fe}(\text{NO})_2$  fragments in complex 1' reveals the delocalization of one unpaired electron between two  $\text{Fe}(\text{NO})_2$  fragments as evidenced by an  $\sim 0.5$  unpaired electron on each  $\text{Fe}(\text{NO})_2$  unit (Fe, +2.47; N1, –0.56; N2, –0.59; O1, –0.45; O2, –0.46), supporting the assignment of electronically delocalized  $\{\text{Fe}(\text{NO})_2\}^9\text{-}\{\text{Fe}(\text{NO})_2\}^{10}$  solid-state  $[\text{Fe}(\text{NO})_2(\mu\text{-bdmap})\text{Fe}(\text{NO})_2]$  (1'). On the other hand, the calculated Fe–N(O)/N–O bond lengths of the four-

Scheme 4. Theoretical Computation for the Hyponitrite-Formation Pathway and NO Disproportionation Pathway via Intermediate  $[\text{Fe}(\text{NO})_2(\mu\text{-bdmap})(\mu\text{-NO})\text{Fe}(\text{NO})_2]$  (A)

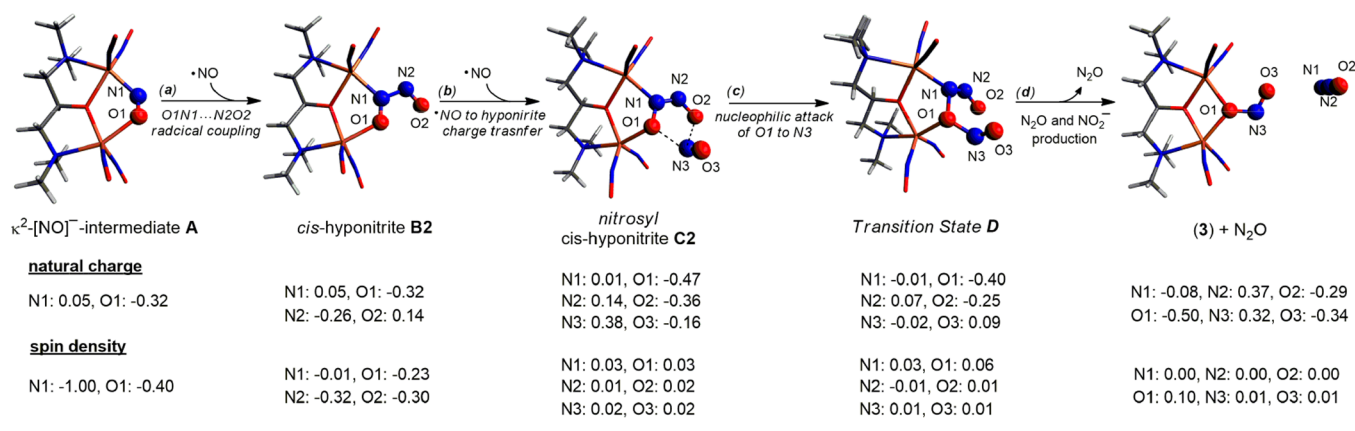


coordinate (4CN)  $\text{Fe}(\text{NO})_2$  and THF-bound five-coordinate (5CN)  $\text{Fe}(\text{NO})_2$  fragments in  $[\text{Fe}(\text{NO})_2(\mu\text{-bdmap})\text{Fe}(\text{NO})_2(\text{THF})]$  (1) demonstrate that the Fe–N(O) bond lengths of the THF-coordinate  $\text{Fe}(\text{NO})_2$  fragment are significantly longer than those of the four-coordinate  $\text{Fe}(\text{NO})_2$  fragment ( $d_{\text{Fe-N}(5\text{CN})} = 1.756 \text{ \AA}$  and  $d_{\text{Fe-N}(4\text{CN})} = 1.631 \text{ \AA}$ ). The strong back-bonding interaction between Fe and NO ligands in the four-coordinate  $\text{Fe}(\text{NO})_2$  fragment is attributed to its electron-rich nature as compared to the THF-bound five-coordinate  $\text{Fe}(\text{NO})_2$  congener. The spin density distribution between 4CN and 5CN  $\text{Fe}(\text{NO})_2$  fragments in complex 1 further reveals the nature of the two  $\text{Fe}(\text{NO})_2$  fragments. Specifically, the 5CN  $\text{Fe}(\text{NO})_2$  fragment exhibits a strong antiferromagnetic coupling interaction between Fe and two coordinated NO ligands, resulting in one unpaired electron situated on the Fe center. Therefore, the electronic structure of the 5CN  $\text{Fe}(\text{NO})_2$  fragment is best described as  $\{\text{Fe}(\text{NO})_2\}^9$ , where the 4CN  $\text{Fe}(\text{NO})_2$  fragment exhibits diamagnetic character which is assigned as  $\{\text{Fe}(\text{NO})_2\}^{10}$  electronic structure. The natural charge analysis on the 4CN and 5CN  $\text{Fe}(\text{NO})_2$  fragments also reveals asymmetric charge distributions between 4CN and 5CN  $\text{Fe}(\text{NO})_2$  fragments ( $\delta_{\text{Fe}(\text{NO})_2-4\text{CN}} = -0.42$  and  $\delta_{\text{Fe}(\text{NO})_2-5\text{CN}} = +0.39$ ). The calculated bond lengths, spin densities, and natural charges of complex 1 support the nature of electronic localization in dinuclear  $\{\text{Fe}(\text{NO})_2\}^{10}-\{\text{Fe}(\text{NO})_2\}^9$  DNIC  $[\text{Fe}(\text{NO})_2(\mu\text{-bdmap})\text{Fe}(\text{NO})_2(\text{THF})]$  (1) resulting from THF coordination to complex 1'.

To unveil the roles of dinuclear DNICs in NO-to- $\text{N}_2\text{O}$  transformation, the reaction mechanism of the intermolecular  $[\text{ON}]^- - [\text{NO}]^-$  coupling pathway to the formation of complex 2 and the NO disproportionation pathway yielding  $[\text{NO}_2]^-$

bridged complex 3 were elucidated by DFT calculations. As indicated from the previous studies,<sup>28b</sup>  $\kappa^2-[\text{NO}]^-$ -bridged  $[\text{Fe}_2(\text{NO})_4(\mu\text{-bdmap})(\mu\text{-NO})]$  (A) plays pivotal roles in facilitating a barrier-free reaction to produce thermodynamically stable hyponitrite-bound intermediate 2 (hyponitrite-formation pathway, Scheme 4). In this study, intermediate A was further demonstrated to proceed via the facile NO disproportionation reaction to form corresponding  $[\text{NO}_2]^-$ -bound complex 3 and  $\text{N}_2\text{O}$  (disproportionation pathway, Scheme 4). Adding 1 equiv of  $\cdot\text{NO}$  to the bridged  $[\text{NO}]^-$  moiety of intermediate A could produce almost isoenergetic *trans*-hyponitrite intermediate B1 and *cis*-hyponitrite intermediate B2 with  $-2.8$  and  $-2.6$  kcal/mol stabilization Gibbs free energies, respectively (Scheme 4a). Unlike the binding of  $\cdot\text{NO}$  to *trans*-hyponitrite intermediate B1 that provides only an additional  $-1.7$  kcal/mol stabilization energy for the formation of nitrosyl *trans*-hyponitrite intermediate C1, the reaction between  $\cdot\text{NO}$  and *cis*-hyponitrite intermediate B2 generates more thermodynamically stable nitrosyl *trans*-hyponitrite intermediate C2 ( $-11.2$  kcal/mol) (Scheme 4b). Intermediate C2 could then proceed to produce corresponding  $[\text{NO}_2]^-$ -bound complex 3 and  $\text{N}_2\text{O}$  via nitrosyl *trans*-hyponitrite transition state D with a 5.8 kcal/mol energy barrier (Scheme 4c,d). The singlet state pathway with a broken-symmetry wave function was evaluated and included in Scheme 3. The singlet state energy of intermediate C2 is only 0.6 kcal/mol higher than that of the corresponding triplet state, which implies that the formation of intermediate C2 possessing a singlet configuration is also energetically accessible as compared to its triplet ground state. In addition, the energies of the broken-symmetry singlet state of transition state D and complex 3 are only 0.3 kcal/mol higher and 0.6 kcal/mol lower, respectively,

Scheme 5. Scheme for the NO Disproportionation Pathway and Spin Density/Natural Charge of Intermediates/Transition States



than those of their corresponding triplet states. The almost isoenergetic nature of the singlet and triplet states among intermediate **C2**, transition state **D**, and complex **3** indicates that the triplet state-to-singlet state transformation is energetically possible along the reaction path from intermediate **C2** to complex **3**, consistent with the experimentally determined singlet ground state of complex **3**. It is noticed that the DFT-optimized geometries and natural charge analysis of intermediate **C2**, transition state **D**, and complex **3** with a broken-symmetry singlet state are almost identical to their triplet counterparts.

The bonding interactions among its three NO ligands of intermediate **C2** could be described as a free NO ligand interacting with the bridging *cis*-hyponitrite moiety of two {Fe(NO)<sub>2</sub>} units. To understand the detailed bonding interactions between the free NO ligand and the metal-bound *cis*-hyponitrite moiety, the selected occupied (HOMO and HOMO - 2) and unoccupied (LUMO and LUMO + 1) orbital contours of the *cis*-hyponitrite fragment as well as the selected occupied (HOMO and HOMO - 1) and unoccupied (LUMO and LUMO + 1) orbital contours of the free NO ligand were depicted (Figure S25a). The key bonding interactions between the free NO ligand and metal-bound *cis*-hyponitrite fragment were obtained by the DFT calculation of intermediate **C2** and revealed by its HOMO - 2  $\alpha$ -spin orbital ( $\alpha$ 118) and LUMO + 7  $\alpha$ -spin orbital ( $\alpha$ 128). The orbital contours of  $\alpha$ 118 and  $\alpha$ 128 indicate that the bonding is best described as a  $\sigma$ -bonding interaction resulting from the formation of a Lewis acid–base adduct between the occupied HOMO - 2 of the metal-bound *cis*-hyponitrite fragment and the unoccupied LUMO ( $\pi^*$  orbital) of the free NO ligand (Figure S25b), consistent with the bonding scheme derived from the natural charge analysis and spin density distribution.

Similar to the hyponitrite-formation pathway (intermediate **A** to complex **2**), the formation of *cis*-hyponitrite (intermediate **A** to intermediate **C2**) in the disproportionation pathway is also barrier-free, downhill by  $\sim$ -13.2 kcal/mol. The energy difference of 10.6 kcal/mol between triplet intermediate **C2** and intermediate **B2** may rationalize the prevention of the back transformation from intermediate **C2** to intermediate **B2**. The computation implicates that the higher NO(g) concentration (>3 equiv) would favor the formation of irreversible and barrier-free *cis*-hyponitrite intermediate **C2** and, subsequently, transform to complex **3** and N<sub>2</sub>O. Under the dilute NO(g) (1 equiv) condition, the formation of either hyponitrite

intermediates (**B1** and **B2**) or *trans*-/*cis*-hyponitrite intermediates (**C1** or **C2**) is limited by the scarcity of NO(g) surrounding intermediate **A**, rationalizing the higher yield of complex **2** under dilute NO(g) (1 equiv) as observed experimentally.

The analysis of natural charge and spin density distributions of the key intermediates, transition state, and the product along the NO disproportionation pathway could provide insights regarding the roles of the dinuclear DNICs in triggering facile N<sub>2</sub>O formation. As compared to the spin density ( $SD_N = 0.72$ ,  $SD_O = 0.28$ ) and natural charge ( $\delta_N = 0.17$ ,  $\delta_O = -0.17$ ) of a free  $\cdot$ NO, the binding of NO to the {Fe(NO)<sub>2</sub>}<sup>10</sup>-{Fe(NO)<sub>2</sub>}<sup>9</sup> core in complex **1** forming intermediate **A** in a  $\kappa^2$ -[NO]<sup>-</sup>-bridged fashion significantly increases the amount of spin density ( $\sim$ 0.4) and polarizes the increased spin density toward the N atom of the  $\kappa^2$ -bridged [NO]<sup>-</sup> moiety as revealed by the analysis of the natural charge and spin density distribution of intermediate **A** ( $SD_{N1} = -1.00$ ,  $SD_{O1} = -0.40$ ;  $\delta_{N1} = 0.05$ ,  $\delta_{O1} = -0.32$ ). The polarized N atom of bridged NO could then proceed via a facile radical-coupling reaction with exogenous  $\cdot$ NO promoting N–N bond formation to yield corresponding *trans*-/*cis*-hyponitrite intermediates **B1**/**B2** (Scheme 5a). Nitrosyl *cis*-hyponitrite intermediate **C2** could be generated by the reaction between *cis*-hyponitrite intermediate **B2** and another equivalent of exogenous  $\cdot$ NO via the electron transfer from the added  $\cdot$ NO to the coordinated *cis*-hyponitrite fragment in **B2**. The intramolecular electron transfer was supported by the positive natural charge ( $\delta_{N3} = 0.38$ ,  $\delta_{O3} = -0.16$ ) and the drastic decrease in spin density ( $SD_{N3} = 0.02$ ,  $SD_{O3} = 0.02$ ) of the N3O3 fragment (the third equiv of added  $\cdot$ NO) in intermediate **C2** (Scheme 5b). The final step in the disproportionation pathway involves the intramolecular rearrangements triggered by the nucleophilic attack of O1 ( $\delta_{O1} = -0.47$ ) on the N3 atom ( $\delta_{N3} = 0.38$ ) of the weakly coordinated [N3O3] group, followed by the subsequent electron redistributions between the coordinated dianionic *cis*-hyponitrite and cation-like [N3O3]<sup>+</sup> fragment to generate final product N<sub>2</sub>O and [NO<sub>2</sub>]<sup>-</sup>-bridged complex **3** (Scheme 5c). The nature of this intramolecular rearrangement could be elaborated by the changes in metric parameters and electronic structures between intermediate **C2** and transition state **D**. The bond distance of O1–N3 is significantly shortened by 0.43 Å (2.03 Å in **C2** and 1.60 Å in **D**), accompanied by a 0.44 Å elongation of the O2–N3 bond distance (1.91 Å in **C2** and 2.35 Å in **D**), which suggests the strong bonding interactions

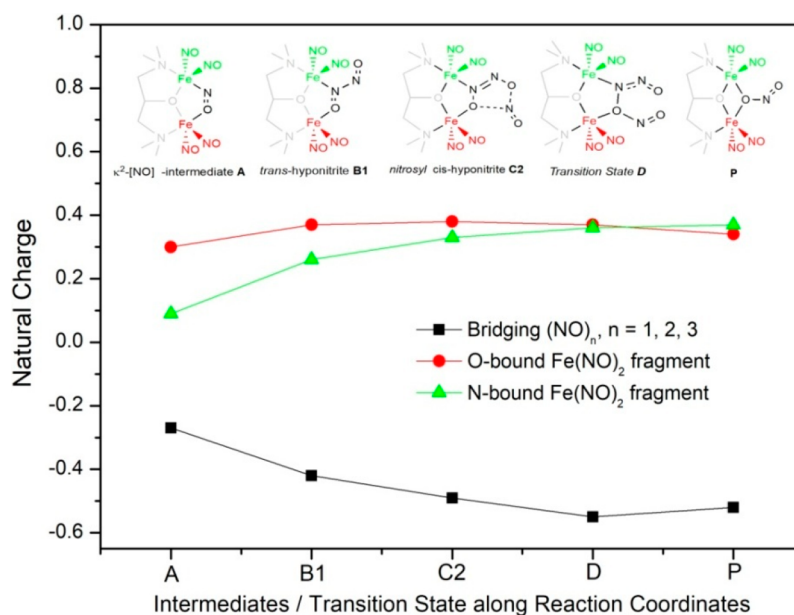


**Figure 8.** Natural charge distributions of bridging  $(\text{NO})_n$  ( $n = 1-3$ ), O-bound  $[\text{Fe}(\text{NO})_2]$ , and N-bound  $[\text{Fe}(\text{NO})_2]$  fragments along the reaction coordinates of the proposed NO disproportionation pathway.

between O1 and N3 from intermediate **C2** to transition state **D** (Scheme 4c). It is important that the same transformation also elongates N1–O1 by 0.43 Å (1.37 Å in **C2** and 1.71 Å in **D**) and concomitantly shortens N1–N2 and N2–O2 by 0.05 and 0.06 Å, respectively, to result in the subsequent N–O bond cleavage as well as  $\text{N}_2\text{O}$  formation. It is noted that the reaction coordinate of this transformation was depicted by the animation of the vibrational movements associated with only one imaginary frequency ( $i = -443 \text{ cm}^{-1}$ ) which is characteristic and a verification of transition state **D** (Figure S26). In addition to the changes in metric parameters, the decrease in the natural charge of the  $[\text{N3O3}]$  fragment (from 0.22 to 0.07) and the increase in the natural charge of the *cis*-hyponitrite fragment (from  $-0.68$  to  $-0.59$ ) in transition state **D** also indicate that the electron-redistribution process between the coordinated *cis*-hyponitrite fragment and the  $\text{N3O3}$  fragment could be facilitated by the nucleophilic attack of O1 on N3.

Complementary to the natural charge distributions of coordinated  $(\text{NO})_n$  ( $n = 1-3$ ) along the reaction coordinates of the disproportionation pathway, the natural charge distributions between the coordinated  $(\text{NO})_n$  ( $n = 1-3$ ) and  $\{\text{Fe}(\text{NO})_2\}$  fragments could provide invaluable insights regarding how dinuclear DNICs modulate their electronic structures during the NO to  $\text{N}_2\text{O}$  transformation. To describe the electron distributions in detail, the  $\{\text{Fe}(\text{NO})_2\}$  fragments of dinuclear DNICs along the reaction coordinates were classified as N-bound  $\{\text{Fe}(\text{NO})_2\}$  and O-bound  $\{\text{Fe}(\text{NO})_2\}$  fragments. As demonstrated in Figure 8, the general trend associated with the increases in electron density on the coordinated  $(\text{NO})_n$  moiety ( $\delta_{(\text{NO})_n}$ ; from  $-0.27$  to  $-0.52$ ) is exactly opposite to the trend associated with the decreases in electron density on the N-bound  $\{\text{Fe}(\text{NO})_2\}$  fragment ( $\delta_{\text{N-bound Fe}(\text{NO})_2}$  = 0.09 to 0.37) along the proposed disproportionation reaction coordinates while the O-bound  $\{\text{Fe}(\text{NO})_2\}$  fragment shows only relatively small perturbations ( $\delta_{\text{O-bound Fe}(\text{NO})_2}$  = 0.30 to 0.34). These results imply that the

two  $\{\text{Fe}(\text{NO})_2\}$  fragments play different roles in modulating the  $(\text{NO})_3$  to  $\text{N}_2\text{O}$  and  $\text{NO}_2^-$  disproportionation reaction. Specifically, the N-bound  $\{\text{Fe}(\text{NO})_2\}$  fragment could act as an electron-transfer channel for supplying one electron that is required for  $\text{NO}_2^-$  formation in order to achieve charge balance, and the O-bound  $\{\text{Fe}(\text{NO})_2\}$  fragment could serve as an electron-buffering reservoir for accommodating electron redistribution processes along the disproportionation reaction coordinates.

## CONCLUSIONS

Nitric oxide (NO) reduction yielding nitrous oxide ( $\text{N}_2\text{O}$ ) triggered by nonheme flavodiiron nitric oxide reductases (FNORs) was reported via the proposed hyponitrite pathway and diferrous dinitrosyl pathway in a biological and biomimetic study.<sup>14–17</sup> In this article, we demonstrated that electronically localized dinuclear  $\{\text{Fe}(\text{NO})_2\}^{10}-\{\text{Fe}(\text{NO})_2\}^9$  DNIC **1** resembling FNORs serves as an NO trapper to facilitate NO reduction to nitrous oxide ( $\text{N}_2\text{O}$ ). Through the direct reaction of  $\text{NO}(\text{g})$  with complex **1** (stoichiometric molar ratio of  $n\text{NO}/\text{complex } 1$  ( $n = 1, 2, 3, 5, \text{ and } 10$ )), the simultaneous formation of *trans*-hyponitrite-bound complex **2**, nitrite-bound complex **3**, and  $\text{N}_2\text{O}$  was observed. The generation of complex **2** as well as complex **3** along with  $\text{N}_2\text{O}$  release, respectively, is attributed to the intermolecular  $[\text{NO}]^- - [\text{NO}]^-$  coupling of relay intermediate  $[\text{Fe}_2(\text{NO})_4(\mu\text{-bdmap})(\mu\text{-NO})]$  (**A**) and NO disproportionation through the sequential binding of exogenous  $\cdot\text{NO}$  to the bridged  $\kappa^2\text{-N}_2\text{O}-[\text{NO}]^-$  of intermediate **A**. That is, the reduction of NO to  $\text{N}_2\text{O}$  triggered by complex **1** occurs via the associated pathways of hyponitrite formation (synthesis cycle: complex **1**  $\rightarrow$  **2**  $\rightarrow$  **5**  $\rightarrow$  **1**) and NO disproportionation (synthesis cycle: complex **1**  $\rightarrow$  **3**  $\rightarrow$  **4**  $\rightarrow$  **5**  $\rightarrow$  **1**) (Scheme 2). Single-crystal X-ray diffraction, EPR/IR spectra, DFT computation, and the electrochemical study of complexes **1/6/7** demonstrate the reversible redox interconversion of  $\{\text{Fe}(\text{NO})_2\}^9 - \{\text{Fe}(\text{NO})_2\}^9$  **7**  $\leftrightarrow$   $\{\text{Fe}(\text{NO})_2\}^{10} - \{\text{Fe}(\text{NO})_2\}^9$  **1**  $\leftrightarrow$   $\{\text{Fe}(\text{NO})_2\}^{10} - \{\text{Fe}(\text{NO})_2\}^{10}$  **6** and characterize the formation of electronically localized  $\{\text{Fe}(\text{NO})_2\}^{10} -$

$\{\text{Fe}(\text{NO})_2\}_2^9$  dinuclear DNIC **1** with THF bound to the  $\{\text{Fe}(\text{NO})_2\}_2^9$  unit with an EPR  $g$  value of 2.013 (THF).<sup>28b</sup> It is presumed that the  $\{\text{Fe}(\text{NO})_2\}_2^9$  unit of DNIC **1** serves as an electron-buffering reservoir to accommodate electron redistribution, and the  $\{\text{Fe}(\text{NO})_2\}_2^{10}$  unit acts as an electron-transfer channel to drive exogenous  $\cdot\text{NO}$  coordination. In addition, the regeneration of DNIC **1** through synthesis cycle (complex **1**  $\rightarrow$  **3**  $\rightarrow$  **4**  $\rightarrow$  **5**  $\rightarrow$  **1**), and alternatively, through synthesis cycle (complex **1**  $\rightarrow$  **2**  $\rightarrow$  **5**  $\rightarrow$  **1**), modulated by the key  $\kappa^2\text{-N,O-}[\text{NO}]^-$ -bridged intermediate **A**, highlights that species **A** acts as a relay intermediate for NO reduction to  $\text{N}_2\text{O}$  via both the hyponitrite formation pathway and the NO disproportionation pathway (Scheme 2).

## EXPERIMENTAL SECTION

Manipulations, reactions, and transfers were conducted under a pure nitrogen atmosphere according to Schlenk techniques or in a glovebox ( $\text{N}_2$  atmosphere). Solvents were purified and distilled under nitrogen by utilizing suitable reagents (acetonitrile from  $\text{CaH}_2\text{-P}_2\text{O}_5$ ; diethyl ether/*n*-hexane/tetrahydrofuran (THF) from sodium benzophenone) and stored in dried,  $\text{N}_2$ -filled flasks over 4 Å molecular sieves. Reagents 1,3-bis(dimethylamino)-2-propanol (Hbdmap) (97% (Sigma-Aldrich)), triflate acid, ferrocenium hexafluorophosphate ( $[\text{Cp}_2\text{Fe}][\text{PF}_6]$ ) (Sigma-Aldrich), and bis(triphenylphosphoranylidene)ammonium chloride ( $[\text{PPN}][\text{Cl}]$ , Fluka) were used as received. Complexes  $[\text{Fe}(\text{CO})_2(\text{NO})_2]$  and  $\{[\text{Fe}(\text{NO})_2]_2(\mu\text{-bdmap})_2\}$  (bdmap = 1,3-bis(dimethylamino)-2-propanoate) were synthesized on the basis of previous reports.<sup>28b</sup> Nitric oxide gas (10% NO + 90%  $\text{N}_2$ ) was purified by passage through a column of Ascarite (8–20 mesh) purchased from Sigma. Infrared spectra (IR) were recorded on a PerkinElmer-Frontier with sealed solution cells (0.1 mm, KBr windows). UV–vis spectra were recorded on an Agilent 8453 spectrophotometer equipped with a UNICOKU liquid  $\text{N}_2$  cryostat.  $^1\text{H}$  NMR spectra were obtained on a Varian Unity-500 MHz spectrometer.  $\text{N}_2\text{O}$  quantification was performed on a Shimadzu GC-2030 gas chromatograph equipped with a barrier-discharge ionization detector (BID). Analyses of carbon, hydrogen, and nitrogen were obtained with a CHN analyzer (Elementar Vario EL III CHN-OS Rapid).

**Preparation of  $[\text{Fe}(\text{NO})_2(\mu\text{-bdmap})\text{Fe}(\text{NO})_2(\text{THF})]$  (**1**).** Freshly prepared complex  $[\text{Fe}(\text{NO})_2(\mu\text{-bdmap})\text{Fe}(\text{NO})_2(\text{THF})]$  (**1**) was synthesized according to published procedures.<sup>28b</sup> IR  $\nu_{\text{NO}}$  1762 m, 1701 s, 1682 sh, 1650 s  $\text{cm}^{-1}$  (THF); 1749 s, 1676 s, 1659 s, 1636 s  $\text{cm}^{-1}$  (KBr). Absorption spectrum (THF)  $[\lambda_{\text{max}} \text{ nm } (\epsilon, \text{M}^{-1} \text{cm}^{-1})]$ : 540 (1090), 755 (1650). EPR spectra show an isotropic signal with  $g = 2.013$  (THF) and  $g = 2.016$  (solid) at 77 K, respectively. The THF solution of complex **1** layered with *n*-hexane (10 mL) was kept at  $-20^\circ\text{C}$  for 1 week, leading to dark-green crystals of  $[\text{Fe}(\text{NO})_2(\mu\text{-bdmap})\text{Fe}(\text{NO})_2]$  characterized by single-crystal X-ray diffraction, as shown in Figure 5a.

**Preparation of  $\{[\text{Fe}_2(\text{NO})_4(\mu\text{-bdmap})_2(\kappa^4\text{-N}_2\text{O}_2)]\}$  (**2**).** Complex  $\{[\text{Fe}_2(\text{NO})_4(\mu\text{-bdmap})_2(\kappa^4\text{-N}_2\text{O}_2)]\}$  (**2**) was synthesized according to the published procedures.<sup>28b</sup> IR 1744 s, 1721 s, 1669 s, 1644 s ( $\nu_{\text{NO}}$ ), 1087 s ( $\nu_{\text{N-O}}([\text{N}_2\text{O}_2]^{2-})$ )  $\text{cm}^{-1}$  (KBr).

**Addition of Various Quantities of NO(g) to a THF Solution of Complex 1 Yielding Complex 2 and  $[\text{Fe}_2(\text{NO})_4(\mu\text{-bdmap})(\mu\text{-NO}_2)]$  (**3**) along with  $\text{N}_2\text{O}$ .** Nitric oxide (74 mL (NO 10% +  $\text{N}_2$  90%), 0.3 mmol) was injected into the freshly prepared THF solution (2 mL) of complex **1** (45 mg (0.1 mmol) stored in a 65 mL vial) by syringe, and the mixture solution was stirred for 3 h at ambient temperature. The mixture solution was then filtered to collect insoluble complex **2** (7.9 mg, yield 19.3  $\pm$  8.7% based on complex **1**), and the brown filtrate was then dried under vacuum to obtain dark-brown solid  $[\text{Fe}_2(\text{NO})_4(\mu\text{-bdmap})(\mu\text{-NO}_2)]$  (**3**) (32.2 mg, 76.2  $\pm$  10.2% based on complex **1**). In a similar fashion, upon addition of 1 equiv of NO to complex **1**, complexes **2** and **3** were obtained in yields of 71.8  $\pm$  7.7 and 25.4  $\pm$  6.9% (47.0  $\pm$  9.1 and 48.6  $\pm$  9.7% yields for the addition of 2 equiv of NO; 14.7  $\pm$  6.3 and 82.7  $\pm$  9.8% yields for

the addition of 5 equiv of NO and 14.3  $\pm$  4.5 and 84.0  $\pm$  8.1% yields for the addition of 10 equiv of NO), respectively. The headspace gas detected by GC and IR  $\nu_{\text{N-N}}$  2223  $\text{cm}^{-1}$  (THF) was characterized as  $\text{N}_2\text{O}$ . On the basis of the IR spectrum ( $\nu_{\text{NO}}$  1762 m, 1701 s, 1682 sh, 1650 s  $\text{cm}^{-1}$ ) of complex **1**, it cannot be ruled out that a trace of residual complex **1** remained in the reaction solution. Attempts to isolate the trace of residual complex **1** were not successful. However, ESI-MS results show the presence of thermodynamically stable complex  $[\text{Fe}_2(\text{NO})_4(\mu\text{-bdmap})_2]$ . Alternatively, complex **1** (0.225 g, 0.5 mmol), potassium nitrite (43 mg, 0.5 mmol), and ferrocenium hexafluorophosphate ( $[\text{Cp}_2\text{Fe}][\text{PF}_6]$ ) (165 mg, 0.5 mmol) prepared in a Schlenk tube were added to THF (5 mL) at  $0^\circ\text{C}$ , leading to the formation of complex **3** (0.179 g, 85%). The THF solution of complex **3** layered with *n*-hexane (10 mL) was kept at  $-20^\circ\text{C}$  for 1 week, leading to dark-brown crystals suitable for X-ray crystallography. IR  $\nu_{\text{NO}}$  1759 s, 1694 s  $\text{cm}^{-1}$  (THF); 1763 sh, 1751 s, 1677 s  $\text{cm}^{-1}$  (KBr). The EPR spectrum shows an isotropic signal of  $g = 2.020$  (solid) at 77 K. Absorption spectrum (THF)  $[\lambda_{\text{max}} \text{ nm } (\epsilon, \text{M}^{-1} \text{cm}^{-1})]$ : 535 (417), 615 (294), 760 (226) at  $30^\circ\text{C}$ ; 790 (261) at  $-80^\circ\text{C}$ . Magnetic susceptibility (solid state (2–300 K):  $\mu_{\text{B}} = 2.75$  (300 K),  $\mu_{\text{B}} = 0.53$  (2 K), and calcd for  $g = 2.030$  and  $J = -45.3 \pm 0.5 \text{ cm}^{-1}$  (antiferromagnetically coupled). Anal. Calcd. for  $\text{C}_7\text{H}_{17}\text{Fe}_2\text{N}_7\text{O}_7$ : C, 19.88; H, 4.05; N, 23.18. Found: C, 20.12; H, 3.96; N, 22.92.

**Quantification of Released  $\text{N}_2\text{O}$  upon Complex 1 Reacted with Various Amounts of NO.**  $\text{N}_2\text{O}$  was quantified on a Shimadzu GC-2030 gas chromatography equipped with a BID detector and ShinCarbon ST (100/120 mesh) columns filled with poly(dimethyl)siloxane (Rtx-1). Helium was adopted as a carrier gas to conduct sample separation. The oven temperature was kept at  $40^\circ\text{C}$  and then increased to  $240^\circ\text{C}$  (rate  $20^\circ\text{C}/\text{min}$ ), and the detector was heated to  $280^\circ\text{C}$ . The identification and quantification of  $\text{N}_2\text{O}$  were achieved by utilizing a gastight syringe to acquire 0.1 mL of sample headspace gas and injected into GC.<sup>28b,35,77</sup> The calibration curves were derived by the injection of various amounts of NO ((10% NO + 90%  $\text{N}_2$ ; 2.2, 4.5, 6.8, 11.2, and 22.4 mL) and pure  $\text{N}_2\text{O}$  (0.10, 0.15, 0.20, 0.30, and 0.50 mL) into a vial (65 mL) containing 2 mL of THF. The calibration curve was plotted in Figure S2. Quantification of the released  $\text{N}_2\text{O}$  is based on gas chromatography with a retention time of 8.14 min. Each vial (65 mL) containing THF solution (2 mL) of complex **1** (4.5 mg, 0.01 mmol) was added to 1 equiv of NO(g) (2.2 mL, (10% NO + 90% $\text{N}_2$ )), 2 equiv of NO (4.5 mL), 3 equiv of NO (6.8 mL), 5 equiv of NO (11.2 mL), and 10 equiv of NO (22.4 mL), individually. The reaction solution was stirred for 3 h, and then the headspace gas (0.1 mL) was injected into the GC for  $\text{N}_2\text{O}$  detection. The average amounts of generated  $\text{N}_2\text{O}$  are displayed in Figure 1b with yields of 23.2  $\pm$  3.54% (injection of 1 equiv of NO), 46.7  $\pm$  9.0% (injection of 2 equiv of NO), 75.8  $\pm$  11.8% (injection of 3 equiv of NO), 84.5  $\pm$  7.2% (injection of 5 equiv of NO), and 87.5  $\pm$  3.5% (injection of 10 equiv of NO) of  $\text{N}_2\text{O}$ .

**Preparation of  $[\text{Fe}_2(\text{NO})_4(\mu\text{-bdmap})(\mu\text{-OCH}_3)]$  (**4**) Derived from the Reaction of Complex 3 and Sodium Methoxide.** Complex **3** (84 mg, 0.2 mmol) and  $[\text{Na}][\text{OMe}]$  (10.8 mg, 0.2 mmol) were added to a Schlenk tube containing 3 mL of THF under an  $\text{N}_2$  atmosphere and stirred for 2 h. The resulting brown solution was filtered through Celite to remove the insoluble solid ( $\text{NaNO}_2$ ), and the brown filtrate was then dried under vacuum to obtain bright-brown solid  $[\text{Fe}_2(\text{NO})_4(\mu\text{-bdmap})(\mu\text{-OCH}_3)]$  (**4**) (isolated yield 72 mg (88.2%). The residual ( $\text{NaNO}_2$ ) was extracted with anaerobic water and was quantified by a Griess test (yield 74.2%). The THF solution of complex **4** was layered with *n*-hexane (15 mL) at  $-20^\circ\text{C}$  for 1 week to produce dark-brown crystals suitable for X-ray crystallography. IR  $\nu_{\text{NO}}$  1743 sh, 1730 s, 1668 s  $\text{cm}^{-1}$  (THF); 1716 s, 1637 s  $\text{cm}^{-1}$  (KBr). Absorption spectrum (THF)  $[\lambda_{\text{max}} \text{ nm } (\epsilon, \text{M}^{-1} \text{cm}^{-1})]$ : 548 (430), 620 (300), and 825 (216). The EPR spectrum shows an isotropic signal with  $g = 2.036$  (solid) at 77 K. Magnetic susceptibility (solid state (2–300 K):  $\mu_{\text{B}} = 2.23$  (300 K),  $\mu_{\text{B}} = 0.89$  (2 K)) and calcd for  $g = 2.035$  and  $J = -172.57 \pm 4.87 \text{ cm}^{-1}$  (antiferromagnetically coupled). Anal. Calcd. for  $\text{C}_8\text{H}_{20}\text{Fe}_2\text{N}_6\text{O}_6$ : C, 23.55; H, 4.94; N, 20.60. Found: C, 23.85; H, 4.97; N, 19.98.

**Protonation of Complex 4 via the Addition of Triflic Acid.** A THF solution (5 mL) containing complex 4 (80.2 mg, 0.2 mmol) was cooled to  $-80\text{ }^{\circ}\text{C}$ , and then a THF solution containing triflic acid (0.2 M, 1 mL) was added to the cooled THF solution of complex 4 drop by drop at  $-80\text{ }^{\circ}\text{C}$ . The resulting dark-green solution was then dried under vacuum to obtain dark-green solid  $[\text{Fe}_2(\text{NO})_4(\mu\text{-bdmap})(\mu\text{-OSO}_2\text{CF}_3)]$  (5) (isolated yield 91 mg (86.5%)). The THF solution of complex 5 was layered with *n*-hexane/diethyl ether (1:1 v/v) at  $-20\text{ }^{\circ}\text{C}$  for 1 week to produce dark-green crystals suitable for X-ray crystallography. IR  $\nu_{\text{NO}}$  1791 sh, 1780 s, 1710 s  $\text{cm}^{-1}$  (THF); 1793 sh, 1785 s, 1705 s, 1685 sh  $\text{cm}^{-1}$  (KBr). Absorption spectrum (THF) [ $\lambda_{\text{max}}$ , nm ( $\epsilon$ ,  $\text{M}^{-1}\text{cm}^{-1}$ ): 540 (430), 610 (385) and 720 (230)]. The EPR spectrum shows an isotropic signal of  $g = 2.034$  (solid) at 77 K. Magnetic susceptibility (solid state (2–300 K)):  $\mu_{\text{B}} = 2.72$  (300 K),  $\mu_{\text{B}} = 0.78$  (2 K) and calcd for  $g = 2.030$  and  $J = -111.1 \pm 1.7\text{ cm}^{-1}$  (antiferromagnetically coupled). Anal. Calcd. for  $\text{C}_8\text{H}_{17}\text{Fe}_2\text{N}_6\text{O}_8\text{F}_3$ : C, 18.27; H, 3.26; N, 15.98. Found: C, 18.15; H, 3.49; N, 15.68.

**Protonation of Complex 2 with Triflic Acid (HOTf).** To complex 2 (81 mg, 0.1 mmol) prepared in a Schlenk tube was added THF (3 mL), and the suspension solution was placed in the Schlenk tube capped with a septum. The prepared THF solution containing HOTf (0.1 M, 2 mL) was then injected into the suspension solution and stirred at  $0\text{ }^{\circ}\text{C}$  for 1 h. The headspace gas and reaction solution were monitored by IR. The  $\nu_{\text{N-N}}$  2223  $\text{cm}^{-1}$  (generation of  $\text{N}_2\text{O}$ ) and  $\nu_{\text{NO}}$  stretching frequencies 1791 sh, 1780 s, 1710 s  $\text{cm}^{-1}$  (formation of 5) that were observed implicated the conversion of complex 2 to 5 along with the release of  $\text{N}_2\text{O}$ . The quantification of  $\text{N}_2\text{O}$  is described below. The injection of headspace gas (0.1 mL) into GC using a gastight syringe after the addition of a THF solution of HOTf (0.1 M, 2 mL) to a THF solution (3 mL) of complex 2 (0.081 g, 0.1 mmol) displays the generation of  $\text{N}_2\text{O}$  (yield 93%).<sup>64</sup> In a similar fashion, the addition of a THF solution of HOTf (0.1 M, 2 mL) to a THF solution (5 mL) of complex 1 (45 mg, 0.1 mmol) at  $0\text{ }^{\circ}\text{C}$  demonstrated the oxidation of 1 to 5 (IR  $\nu_{\text{NO}}$  1791 sh, 1780 s, 1710 s  $\text{cm}^{-1}$ ) along with  $\text{H}_2$  release (detected by GC).

**Reaction of Complex 5 and Bis(benzene)chromium (CrBz<sub>2</sub>).** Complex 5 (53 mg, 0.1 mmol) and bis(benzene)chromium (20.8 mg, 0.1 mmol) were added to a Schlenk tube containing 3 mL of THF under an  $\text{N}_2$  atmosphere, and then the reaction solution that was gradually converted to a dark-blue solution was observed after the reaction solution was stirred for 30 min at ambient temperature. IR  $\nu_{\text{NO}}$  stretching frequencies 1762 m, 1701 s, 1682 sh, and 1650 s  $\text{cm}^{-1}$  (THF) demonstrated the formation of dinuclear  $\{\text{Fe}(\text{NO})_2\}^9\text{-}\{\text{Fe}(\text{NO})_2\}^{10}$  DNIC 1.

**Reaction of Complex 1 and  $\text{KC}_8$  + [PPN][Cl].** Complex 1 (45 mg, 0.1 mmol) and  $\text{KC}_8$  (13.5 mg, 0.1 mmol) were added to a Schlenk tube containing 3 mL of THF in a glovebox. The THF solution was transferred to a  $\text{CH}_3\text{CN}$  solution (1 mL) of [PPN][Cl] (57.4 mg, 0.1 mmol), and the THF- $\text{CH}_3\text{CN}$  mixture solution was then stirred for 2 h at ambient temperature. The resulting green solution was filtered through Celite to remove the insoluble solid (KCl and graphite), and the green filtrate was dried under vacuum to obtain diamagnetic greenish-yellow solid [PPN] $[\text{Fe}_2(\text{NO})_4(\mu\text{-bdmap})]$  (6). The THF- $\text{CH}_3\text{CN}$  solution of complex 6 was layered with diethyl ether (10 mL) at ambient temperature for 2 weeks to produce greenish-yellow crystals suitable for X-ray crystallography (yield 58 mg (65.8%)). IR  $\nu_{\text{NO}}$  1671 s, 1657 sh, 1613 s  $\text{cm}^{-1}$  (THF); 1664 s, 1603 s  $\text{cm}^{-1}$  (KBr). Absorption spectrum (THF) [ $\lambda_{\text{max}}$ , nm ( $\epsilon$ ,  $\text{M}^{-1}\text{cm}^{-1}$ ): 405 (1440), 750 (132)].  $^1\text{H NMR}$ :  $\delta$  7.68–7.48 (m, Ar-CH), 4.54 (O-CH), 2.56 (– $\text{CH}_2$ –), 2.33 (N- $\text{CH}_3$ ) ppm at 298 K ( $\text{CD}_3\text{CN}$ ). Anal. Calcd. for  $\text{C}_{43}\text{H}_{47}\text{Fe}_2\text{N}_7\text{O}_5\text{P}_2$ : C, 56.41; H, 5.17; N, 10.71. Found: C, 56.12; H, 5.32; N, 10.31.

**Oxidation of Complex 6 with Silver Triflate (AgOTf).** A suspended THF solution (5 mL) containing complex 6 (45.5 mg, 0.05 mmol) was added to a Schlenk tube containing 1 equiv of silver triflate (12.8 mg, 0.05 mmol) under a  $\text{N}_2$  atmosphere. The reaction solution was stirred for 1 h and gradually converted to a dark-blue solution at  $0\text{ }^{\circ}\text{C}$ . IR  $\nu_{\text{NO}}$  stretching frequencies 1762 m, 1701 s, 1682 sh, and 1650 s  $\text{cm}^{-1}$  (THF) demonstrated the formation of the known  $\{\text{Fe}(\text{NO})_2\}^9\text{-}\{\text{Fe}(\text{NO})_2\}^{10}$  dinuclear DNIC  $[\text{Fe}(\text{NO})_2(\mu\text{-$

bdmap) $\text{Fe}(\text{NO})_2(\text{THF})]$  (1), as shown in Figure 6. Subsequently, the second equivalent of silver triflate was added to a dark-blue solution (complex 1), leading to a dark-green solution. IR  $\nu_{\text{NO}}$  stretching frequencies 1791 sh, 1780 s, and 1710 s  $\text{cm}^{-1}$  (THF) demonstrated the formation of dinuclear  $\{\text{Fe}(\text{NO})_2\}^9\text{-}\{\text{Fe}(\text{NO})_2\}^9$  DNIC  $[\text{Fe}_2(\text{NO})_4(\mu\text{-bdmap})(\mu\text{-OSO}_2\text{CF}_3)]$  (5), as shown in Figure 6.

**Oxidation of Complex 1 with Ferrocenium Hexafluorophosphate ( $[\text{Cp}_2\text{Fe}][\text{PF}_6]$ ).** Ferrocenium hexafluorophosphate (100 mg, 0.1 mmol) and complex 1 (135 mg, 0.3 mmol) were added to a Schlenk tube containing 2 mL of THF in a glovebox, and then the reaction solution was gradually converting to a dark-green solution after the reaction solution was stirred for 1 h at  $0\text{ }^{\circ}\text{C}$ . IR  $\nu_{\text{NO}}$  1790 sh, 1776 s, 1710 s  $\text{cm}^{-1}$  (THF) and 1783 s, 1771 s, and 1703 s  $\text{cm}^{-1}$  (KBr) suggested the formation of dinuclear  $\{\text{Fe}(\text{NO})_2\}^9\text{-}\{\text{Fe}(\text{NO})_2\}^9$  DNIC  $[\text{Fe}_2(\text{NO})_4(\mu\text{-bdmap})(\mu\text{-THF})][\text{PF}_6]$  (7), as shown in Figure S19. The THF solution of complex 7 was layered with *n*-hexane (10 mL) at ambient temperature for 2 weeks to produce brownish-green crystals suitable for X-ray crystallography (crystal yield 96 mg (53.8%)). Absorption spectrum (THF) [ $\lambda_{\text{max}}$ , nm ( $\epsilon$ ,  $\text{M}^{-1}\text{cm}^{-1}$ ): 545 (450), 608 (510), 740 (185)]. The EPR spectrum shows an isotropic signal of  $g = 2.037$  (solid) at 77 K. Magnetic susceptibility (solid state (2–300 K)):  $\mu_{\text{B}} = 2.73$  (300 K),  $\mu_{\text{B}} = 0.86$  (2 K), and calcd for  $g = 2.030$  and  $J = -122.2 \pm 2.4\text{ cm}^{-1}$  (antiferromagnetically coupled). Anal. Calcd. for  $\text{C}_{11}\text{H}_{25}\text{Fe}_2\text{N}_6\text{O}_6\text{F}_6\text{P}_1$ : C, 22.24; H, 4.24; N, 14.15. Found: C, 21.83; H, 4.18; N, 13.67.

**Cyclic Voltammetry Measurements.** Electrochemical measurements were recorded on a CH Instruments 621E electrochemical potential state using a gastight three-electrode cell under  $\text{N}_2$  at room temperature. A glassy carbon electrode (3 mm in diameter) and a platinum wire were used as the working and counter electrodes, respectively. The reference electrode was a nonaqueous  $\text{Ag}/\text{Ag}^+$  electrode. Cyclic voltammograms were obtained from 2.0 mM analyte concentration in  $\text{O}_2$ -free THF using 0.2 M electrolyte (*n*-tetrabutylammonium hexafluorophosphate). All potentials are reported toward ferrocene/ferrocenium ( $\text{Fc}/\text{Fc}^+$ ).

**Crystallography.** The single-crystal X-ray crystallographic data collections for complexes 1 and 3–7 were carried out at 200 K with a Bruker D8 venture dual X-ray single-crystal diffractometer with graphite-monochromated Mo  $K\alpha$  radiation ( $\lambda = 0.71073\text{ \AA}$ ) outfitted with a low-temperature, nitrogen-stream aperture. The structures were solved by direct methods, in conjunction with standard difference Fourier techniques and refined by full-matrix least-squares procedures. Least-squares refinement of the positional and anisotropic thermal parameters of all non-hydrogen atoms and fixed hydrogen atoms was carried out with the riding model.<sup>78</sup> The SHELXTL structure refinement program was employed.<sup>79</sup> A summary of the crystallographic parameters for complexes 1 and 3–7 are shown in Tables S2 and S3.

**EPR Measurements.** The X-band EPR measurements were recorded at 77 K on a Bruker E580 CW/pulse EPR equipped with an Oxford liquid-He quartz cryostat. The EPR samples (solution and powder) of complexes 3, 4, 5, and 7 were transferred to EPR tubes and then immediately frozen in liquid nitrogen prior to measurements. The experimental parameters are the following: microwave frequency = 9.657 GHz, microwave power = 15 mW, modulation amplitude = 1.6 mT, modulation frequency = 100 kHz, gain = 30, and time constant = 3276.8 ms.

**Magnetic Measurements.** The magnetic data of the microcrystalline samples of complexes 3, 4, 5, and 7 were placed in a polycarbonate capsule and were recorded on a SQUID magnetometer (SQUID-VSM, Quantum Design) under an external magnetic field (0.5 T) in the temperature range of 2–300 K. The magnetic susceptibility data were corrected with the ligand diamagnetism by the tabulated Pascal constants<sup>80a</sup> and the sample holder. It is assumed that the electronic structure for complexes 3–5 and 7 are best described as  $\{\text{Fe}(\text{NO})_2\}^9\text{-}(\mu\text{-OR})_2\text{-}\{\text{Fe}(\text{NO})_2\}^9$ . The spin Hamiltonian ( $\hat{H}_1 = -J\hat{S}_1\hat{S}_2$ ) is used to illustrate the weak magnetic coupling (dipolar coupling) between two  $\{\text{Fe}(\text{NO})_2\}^9$  centers.<sup>80b</sup> These analyses were performed by taking the product of the magnetic

susceptibility ( $\chi_M$ ) and the absolute temperature ( $T$ ) as a function of the absolute temperature and fitting the data to the Boltzmann distribution.

**XAS Measurements.** All Fe K-edge spectra were completed at the National Synchrotron Radiation Research Center (NSRRC), Hsinchu, Taiwan. The measurements were carried out at the TPS 44A beamline (quick-scanning X-ray absorption spectroscopy, 4.5–34 keV) with a double-crystal Si(111) monochromator and were recorded at room temperature. The energy resolution  $\Delta E/E$  was estimated to be about  $2 \times 10^{-4}$ . High harmonics were rejected by Rh-coated mirrors. Ion chambers used to measure the incident ( $I_0$ ) and transmitted ( $I$ ) beam intensities were filled with a mixture of  $N_2$  and He gases and a mixture of  $N_2$  and Ar gases, respectively. The spectra were scanned from 6.912 to 8.006 keV. The energy calibration was referenced by measuring, simultaneously, the iron foil (the first inflection point at 7112.0 eV). The energy resolution of 0.3 eV can be achieved. A smooth background was removed from all spectra by fitting a straight line to the pre-edge region and then subtracting this straight line from the entire spectrum. Normalization of the data was accomplished by fitting a flat polynomial to the postregion and also normalizing the edge jump to 1.0 at 7400 eV for Fe K-edge spectra.<sup>81</sup>

**Computational Details.** The initial coordinates for geometry optimizations of **2** and **3** were taken from single-crystal X-ray crystallography data. The coordinates of intermediate **A** were taken from previous studies.<sup>28b</sup> All geometry optimization DFT calculations were conducted with the TZVP basis set<sup>82</sup> for Fe, N, and O and with the 6-31G\* basis set<sup>83</sup> for C and H (ultrafine integration grid and very tight SCF criteria) by Gaussian 16, version B01.<sup>84</sup> Meta-GGA functional TPSSH<sup>85</sup> was used to obtain the geometry-optimized DFT structures of **2**, **3**, all intermediates, and the transition state. The vibrational analysis verified the optimized DFT structures of **2** and **3**, and intermediates are either stationary points or true minima on the potential energy hypersurface. The transition state was confirmed by the existence of one negative frequency as well as the internal reaction coordinate (IRC) calculations. The calculations of the single-point energy and the Gibbs free energy profile were conducted under the same basis set and functionals used in geometry optimization with a PCM solvent correction<sup>86</sup> for the solvent used in experiments. The diffusion correction for TPSSH was also included in the single-point energy, frequency, and Gibbs free energy calculations.<sup>87</sup> The natural population analysis and orbital contour plots were obtained with NBO 3.1<sup>88</sup> and Avogadro,<sup>89</sup> respectively.

## ■ ASSOCIATED CONTENT

### SI Supporting Information

The Supporting Information is available free of charge at <https://pubs.acs.org/doi/10.1021/acs.inorgchem.1c00541>.

Details of spectroscopic data (FTIR, EPR, CV, and XAS) and X-ray diffraction data collection (PDF)

### Accession Codes

CCDC 2057454–2057458 and 2057461 contain the supplementary crystallographic data for this paper. These data can be obtained free of charge via [www.ccdc.cam.ac.uk/data\\_request/cif](http://www.ccdc.cam.ac.uk/data_request/cif), or by emailing [data\\_request@ccdc.cam.ac.uk](mailto:data_request@ccdc.cam.ac.uk), or by contacting The Cambridge Crystallographic Data Centre, 12 Union Road, Cambridge CB2 1EZ, UK; fax: +44 1223 336033. CCDC 2057454 for **1'**, 2057455 for **3**, 2057456 for **4**, 2057457 for **5**, 2057458 for **6**, and 2057461 for **7** contain the supplementary crystallographic data for this paper. These data can be obtained free of charge via [www.ccdc.cam.ac.uk/data\\_request/cif](http://www.ccdc.cam.ac.uk/data_request/cif), or by emailing [data\\_request@ccdc.cam.ac.uk](mailto:data_request@ccdc.cam.ac.uk), or by contacting The Cambridge Crystallographic Data Centre, 12 Union Road, Cambridge CB2 1EZ, UK; fax: + 44 1223 336033.

## ■ AUTHOR INFORMATION

### Corresponding Authors

Ming-Li Tsai – Department of Chemistry, National Sun Yat-sen University, Kaohsiung 80424, Taiwan; [orcid.org/0000-0003-2510-2866](https://orcid.org/0000-0003-2510-2866); Email: [mltsai@mail.nsysu.edu.tw](mailto:mltsai@mail.nsysu.edu.tw)

Wen-Feng Liaw – Department of Chemistry and Frontier Research Center of Fundamental and Applied Science of Matters, National Tsing Hua University, Hsinchu 30013, Taiwan; [orcid.org/0000-0001-9949-8344](https://orcid.org/0000-0001-9949-8344); Email: [wfliaw@mx.nthu.edu.tw](mailto:wfliaw@mx.nthu.edu.tw)

### Authors

Wun-Yan Wu – Department of Chemistry and Frontier Research Center of Fundamental and Applied Science of Matters, National Tsing Hua University, Hsinchu 30013, Taiwan; [orcid.org/0000-0003-3812-3981](https://orcid.org/0000-0003-3812-3981)

Yi-An Lai – Department of Chemistry and Frontier Research Center of Fundamental and Applied Science of Matters, National Tsing Hua University, Hsinchu 30013, Taiwan

Chieh-Hsin Hsieh – Department of Chemistry and Frontier Research Center of Fundamental and Applied Science of Matters, National Tsing Hua University, Hsinchu 30013, Taiwan

Complete contact information is available at: <https://pubs.acs.org/10.1021/acs.inorgchem.1c00541>

### Notes

The authors declare no competing financial interest.

## ■ ACKNOWLEDGMENTS

We gratefully acknowledge financial support from the Ministry of Science and Technology and the Featured Area Research Center Program within the framework of the Higher Education Sprout Project by the Ministry of Education (MOE) (Taiwan). We also thank the National Synchrotron Radiation Research Center (NSRRC, Taiwan) and the National Center for High-Performance Computing for their support of the hardware and software applied in this work. The authors thank Ms. Pei-Lin Chen (NTHU) and Mr. Ting-Shen Kuo (NTNU) for single-crystal X-ray structural determinations and Dr. Fu-Te Tsai (NTHU) and Dr. I-Jui Hsu (NTUT) for help with XAS. The authors thank the Instrumentation Center at NTHU for providing the EPR and SQUID analysis and the Instrument Center at NCHU for providing valuable assistance with elemental analysis.

## ■ REFERENCES

- (1) Ignarro, L. *Nitric Oxide: Biology and Pathobiology*; Academic Press: San Diego, 2000.
- (2) Pacher, P.; Beckman, J. S.; Liaudet, L. Nitric oxide and peroxynitrite in health and disease. *Physiol. Rev.* **2007**, *87*, 315–424.
- (3) Bogdan, C. Nitric Oxide and the Immune Response. *Nat. Immunol.* **2001**, *2*, 907–916.
- (4) Wasser, I. M.; de Vries, S.; Moënne-Loccoz, P.; Schröder, L.; Karlin, K. D. Nitric Oxide in Biological Denitrification: Fe/Cu Metalloenzyme and Metal Complex  $NO_x$  Redox Chemistry. *Chem. Rev.* **2002**, *102*, 1201–1234.
- (5) Ferousi, C.; Majer, S. H.; DiMucci, I. M.; Lancaster, K. M. Biological and Bioinspired Inorganic N–N Bond-Forming Reactions. *Chem. Rev.* **2020**, *120*, 5252–5307.
- (6) Shiro, Y. Structure and function of bacterial nitric oxide reductases: Nitric oxide reductase, anaerobic enzymes. *Biochim. Biophys. Acta, Bioenerg.* **2012**, *1817*, 1907–1913.

(7) Hino, T.; Matsumoto, Y.; Nagano, S.; Sugimoto, H.; Fukumori, Y.; Murata, T.; Iwata, S.; Shiro, Y. Structural Basis of Biological N<sub>2</sub>O Generation by Bacterial Nitric Oxide Reductase. *Science* **2010**, *330*, 1666.

(8) Khatua, S.; Majumdar, A. Flavodiiron nitric oxide reductases: Recent developments in the mechanistic study and model chemistry for the catalytic reduction of NO. *J. Inorg. Biochem.* **2015**, *142*, 145–153.

(9) Moëne-Loccoz, P. Spectroscopic characterization of heme iron–nitrosyl species and their role in NO reductase mechanisms in diiron proteins. *Nat. Prod. Rep.* **2007**, *24*, 610–620.

(10) Kurtz, D. M., Jr. Flavo-diiron enzymes: nitric oxide or dioxygen reductases? *Dalton Trans.* **2007**, 4115–4121.

(11) Silaghi-Dumitrescu, R.; Kurtz, D. M., Jr.; Ljungdahl, L.; Lanzilotta, W. N. A Flavo-Diiron Protein from *Desulfovibrio vulgaris* with Oxidase and Nitric Oxide Reductase Activities. Evidence for an in Vivo Nitric Oxide Scavenging Function†. *Biochemistry* **2005**, *44*, 3572–3579.

(12) Hayashi, T.; Caranto, J. D.; Wampler, D. A.; Kurtz, D. M.; Moëne-Loccoz, P. Insights into the Nitric Oxide Reductase Mechanism of Flavodiiron Proteins from a Flavin-Free Enzyme. *Biochemistry* **2010**, *49*, 7040–7049.

(13) Lo, F.-C.; Hsieh, C.-C.; Maestre-Reyna, M.; Chen, C.-Y.; Ko, T.-P.; Horng, Y.-C.; Lai, Y.-C.; Chiang, Y.-W.; Chou, C.-M.; Chiang, C.-H.; Huang, W.-N.; Lin, Y.-H.; Bohle, D. S.; Liaw, W.-F. Crystal Structure Analysis of the Repair of Iron Centers Protein YtfE and Its Interaction with NO. *Chem. - Eur. J.* **2016**, *22*, 9768–9776.

(14) Blomberg, L. M.; Blomberg, M. R.; Siegbahn, P. E. Theoretical Study of the Reduction of Nitric Oxide in an  $\alpha$ -Type Flavoprotein. *JBIC, J. Biol. Inorg. Chem.* **2006**, *12*, 79–89.

(15) Caranto, J. D.; Weitz, A.; Hendrich, M. P.; Kurtz, D. M. The Nitric Oxide Reductase Mechanism of a Flavo-Diiron Protein: Identification of Active-Site Intermediates and Products. *J. Am. Chem. Soc.* **2014**, *136*, 7981–7992.

(16) (a) Weitz, A. C.; Giri, N.; Frederick, R. E.; Kurtz, D. M., Jr.; Bominaar, E. L.; Hendrich, M. P. Spectroscopy and DFT Calculations of Flavodiiron Nitric Oxide Reductase Identify Bridging Structures of NO-Coordinated Diiron Intermediates. *ACS Catal.* **2018**, *8*, 11704–11715. (b) Lu, J.; Bi, B.; Lai, W.; Chen, H. Origin of Nitric Oxide Reduction Activity in Flavo-Diiron NO Reductase: Key Roles of Second Coordination Sphere. *Angew. Chem.* **2019**, *131*, 3835.

(17) Enemark, J. H.; Feltham, R. D. Principles of Structure, Bonding, and Reactivity for Metal Nitrosyl Complexes. *Coord. Chem. Rev.* **1974**, *13*, 339–406.

(18) Collman, J. P.; Yang, Y.; Dey, A.; Decréau, R. A.; Ghosh, S.; Ohta, T.; Solomon, E. I. A functional nitric oxide reductase model. *Proc. Natl. Acad. Sci. U. S. A.* **2008**, *105*, 15660–15665.

(19) Wang, J.; Schopfer, M. P.; Puiui, S. C.; Sarjeant, A. A. N.; Karlin, K. D. Reductive Coupling of Nitrogen Monoxide ( $\cdot$ NO) Facilitated by Heme/Copper Complexes. *Inorg. Chem.* **2010**, *49*, 1404–1419.

(20) Berto, T. C.; Speelman, A. L.; Zheng, S.; Lehnert, N. Mono- and Dinuclear Non-Heme Iron–Nitrosyl Complexes: Models for Key Intermediates in Bacterial Nitric Oxide Reductases. *Coord. Chem. Rev.* **2013**, *257*, 244–259.

(21) Zheng, S.; Berto, T. C.; Dahl, E. W.; Hoffman, M. B.; Speelman, A. L.; Lehnert, N. The Functional Model Complex [Fe<sub>2</sub>(BPMP)(OPr)(NO)<sub>2</sub>](BPh<sub>4</sub>)<sub>2</sub> Provides Insight into the Mechanism of Flavodiiron NO Reductases. *J. Am. Chem. Soc.* **2013**, *135*, 4902–4905.

(22) Jiang, Y.; Hayashi, T.; Matsumura, H.; Do, L. H.; Majumdar, A.; Lippard, S. J.; Moëne-Loccoz, P. Light-Induced N<sub>2</sub>O Production from a Non-Heme Iron-Nitrosyl Dimer. *J. Am. Chem. Soc.* **2014**, *136*, 12524–12527.

(23) (a) Dong, H. T.; White, C. J.; Zhang, B.; Krebs, C.; Lehnert, N. Non-Heme Diiron Model Complexes Can Mediate Direct NO Reduction: Mechanistic Insight into Flavodiiron NO Reductases. *J. Am. Chem. Soc.* **2018**, *140*, 13429–13440. (b) White, C. J.; Speelman, A. L.; Kupper, C.; Demeshko, S.; Meyer, F.; Shanahan, J. P.; Alp, E. E.; Hu, M.; Zhao, J.; Lehnert, N. The Semireduced Mechanism for

Nitric Oxide Reduction by Non-Heme Diiron Complexes: Modeling Flavodiiron Nitric Oxide Reductases. *J. Am. Chem. Soc.* **2018**, *140*, 2562–2574.

(24) (a) Jana, M.; Pal, N.; White, C. J.; Kupper, C.; Meyer, F.; Lehnert, N.; Majumdar, A. Functional Mononitrosyl Diiron(II) Complex Mediates the Reduction of NO to N<sub>2</sub>O with Relevance for Flavodiiron NO Reductases. *J. Am. Chem. Soc.* **2017**, *139*, 14380–14383. (b) Jana, M.; White, C. J.; Pal, N.; Demeshko, S.; Cordes, C.; Meyer, F.; Lehnert, N.; Majumdar, A. Functional Models for the Mono- and Di-nitrosyl Intermediates of FNORs: Semireduction versus Superreduction of NO. *J. Am. Chem. Soc.* **2020**, *142*, 6600–6616.

(25) Confer, A. M.; McQuilken, A. C.; Matsumura, H.; Moëne-Loccoz, P.; Goldberg, D. P. A Nonheme, High-Spin {FeNO}<sup>8</sup> Complex that Spontaneously Generates N<sub>2</sub>O. *J. Am. Chem. Soc.* **2017**, *139*, 10621–10624.

(26) Bar, A. M.; Ojea, M. J. H.; Tang, J.; Layfield, R. A. Coupling of Nitric Oxide and Release of Nitrous Oxide from Rare-Earth-Dinitrosyliron Complexes. *J. Am. Chem. Soc.* **2020**, *142* (9), 4104–4107.

(27) Wright, A. M.; Hayton, T. W. Understanding the Role of Hyponitrite in Nitric Oxide Reduction. *Inorg. Chem.* **2015**, *54*, 9330–9341.

(28) (a) Wu, W.-Y.; Liaw, W.-F. Nitric oxide reduction forming hyponitrite triggered by metal-containing complexes. *J. Chin. Chem. Soc.* **2020**, *67*, 206–212. (b) Wu, W.-Y.; Hsu, C.-N.; Hsieh, C.-H.; Chiou, T.-W.; Tsai, M.-L.; Chiang, M.-H.; Liaw, W.-F. NO-to-[N<sub>2</sub>O<sub>2</sub>]<sup>2-</sup>-to-N<sub>2</sub>O Conversion Triggered by {Fe(NO)<sub>2</sub>}<sup>10</sup>-{Fe(NO)<sub>2</sub>}<sup>9</sup> Dinuclear Dinitrosyl Iron Complex. *Inorg. Chem.* **2019**, *58* (15), 9586–9591.

(29) Arikawa, Y.; Asayama, T.; Moriguchi, Y.; Agari, S.; Onishi, M. Reversible N–N Coupling of NO Ligands on Dinuclear Ruthenium Complexes and Subsequent N<sub>2</sub>O Evolution: Relevance to Nitric Oxide Reductase. *J. Am. Chem. Soc.* **2007**, *129*, 14160–14161.

(30) Wright, A. M.; Wu, G.; Hayton, T. W. Formation of N<sub>2</sub>O from a Nickel Nitrosyl: Isolation of the cis-[N<sub>2</sub>O<sub>2</sub>]<sup>2-</sup> Intermediate. *J. Am. Chem. Soc.* **2012**, *134*, 9930–9933.

(31) (a) Lionetti, D.; de Ruiter, G.; Agapie, T. A trans-Hyponitrite Intermediate in the Reductive Coupling and Deoxygenation of Nitric Oxide by a Tricopper–Lewis Acid Complex. *J. Am. Chem. Soc.* **2016**, *138*, 5008–5011. (b) Hosseiniasab, V.; McQuilken, A. C.; Bakhoda, A.; Bertke, J. A.; Timerghazin, Q. K.; Warren, T. H. Lewis Acid Coordination Redirects S-Nitrosothiol Signaling Output. *Angew. Chem., Int. Ed.* **2020**, *59*, 10854–10858.

(32) Wijeratne, G. B.; Hematian, S.; Siegler, M. A.; Karlin, K. D. Copper(I)/NO(g) Reductive Coupling Producing a trans-Hyponitrite Bridged Dicopper(II) Complex: Redox Reversal Giving Copper-(I)/NO(g) Disproportionation. *J. Am. Chem. Soc.* **2017**, *139*, 13276–13279.

(33) Chuang, C.-H.; Liaw, W.-L.; Hung, C.-H. Conversion of Nitric Oxide into Nitrous Oxide as Triggered by the Polarization of Coordinated NO by Hydrogen Bonding. *Angew. Chem., Int. Ed.* **2016**, *55*, 5190–5194.

(34) Evans, W. J.; Fang, M.; Bates, J. E.; Furche, F.; Ziller, J. W.; Kiesz, M. D.; Zink, J. I. Isolation of a radical dianion of nitrogen oxide (NO)<sup>2-</sup>. *Nat. Chem.* **2010**, *2*, 644–647.

(35) Kundu, S.; Phu, P. N.; Ghoah, P.; Kozimor, S. A.; Bertke, J. A.; Stieber, S. C. E.; Warren, T. H. Nitrosyl Linkage Isomers: NO Coupling to N<sub>2</sub>O at a Mononuclear Site. *J. Am. Chem. Soc.* **2019**, *141*, 1415–1419.

(36) Ferretti, E.; Dechert, S.; Demeshko, S.; Holthausen, M. C.; Meyer, F. Reductive Nitric Oxide Coupling at a Dinickel Core: Isolation of a Key cis-Hyponitrite Intermediate en route to N<sub>2</sub>O Formation. *Angew. Chem., Int. Ed.* **2019**, *58*, 1705–1709.

(37) (a) Abucayon, E. G.; Khade, R. L.; Powell, D. R.; Zhang, Y.; Richter-Addo, G. B. Lewis Acid Activation of the Ferrous Heme–NO Fragment toward the N–N Coupling Reaction with NO To Generate N<sub>2</sub>O. *J. Am. Chem. Soc.* **2018**, *140* (12), 4204–4207. (b) Abucayon, E. G.; Khade, R. L.; Powell, D. R.; Zhang, Y.; Richter-Addo, G. B. Not

Limited to Iron: A Cobalt Heme–NO Model Facilitates N–N Coupling with External NO in the Presence of a Lewis Acid to Generate N<sub>2</sub>O. *Angew. Chem.* **2019**, *131*, 18771–18776.

(38) (a) Brozek, C. K.; Miller, J. T.; Stoian, S. A.; Dincă, M. NO Disproportionation at a Mononuclear Site-Isolated Fe<sup>2+</sup> Center in Fe<sup>2+</sup>-MOF-5. *J. Am. Chem. Soc.* **2015**, *137*, 7495–7501. (b) Jover, J.; Brozek, C. K.; Dincă, M.; López, N. Computational Exploration of NO Single-Site Disproportionation on Fe-MOF-5. *Chem. Mater.* **2019**, *31*, 8875–8885. (c) Sun, C.; Yang, L.; Ortuño, M. A.; Wright, A. M.; Chen, T.; Head, A. R.; López, N.; Dincă, M. Spectroscopic Evidence of Hyponitrite Radical Intermediate in NO Disproportionation at a MOF-Supported Mononuclear Copper Site. *Angew. Chem., Int. Ed.* **2021**, *60*, 7845–7850.

(39) Franz, K. J.; Lippard, S. J. NO Disproportionation Reactivity of Fe Tropocoronand Complexes. *J. Am. Chem. Soc.* **1999**, *121*, 10504–10512.

(40) Martirosyan, G. G.; Azizyan, A. S.; Kurtikyan, T. S.; Ford, P. C. Low temperature NO disproportionation by Mn porphyrin. Spectroscopic characterization of the unstable nitrosyl nitrito complex Mn<sup>III</sup>(TPP)(NO)(ONO). *Chem. Commun.* **2004**, 1488–1489.

(41) Patra, A. K.; Rose, M. J.; Olmstead, M. M.; Mascharak, P. K. Reactions of Nitric Oxide with a Low-Spin Fe(III) Center Ligated to a Tetradentate Dicarboxamide N<sub>4</sub> Ligand: Parallels between Heme and Non-heme Systems. *J. Am. Chem. Soc.* **2004**, *126*, 4780–4781.

(42) Schneider, J. L.; Carrier, S. M.; Ruggiero, C. E.; Young, V. G.; Tolman, W. B. Influences of Ligand Environment on the Spectroscopic Properties and Disproportionation Reactivity of Copper–Nitrosyl Complexes. *J. Am. Chem. Soc.* **1998**, *120*, 11408–11418.

(43) Metz, S. N<sub>2</sub>O Formation via Reductive Disproportionation of NO by Mononuclear Copper Complexes: A Mechanistic DFT Study. *Inorg. Chem.* **2017**, *56*, 3820–3833.

(44) Azizyan, A. S.; Kurtikyan, T. S.; Martirosyan, G. G.; Ford, P. C. Tracking Reactive Intermediates by FTIR Monitoring of Reactions in Low-Temperature Sublimed Solids: Nitric Oxide Disproportionation Mediated by Ruthenium(II) Carbonyl Porphyrin Ru(TPP)(CO). *Inorg. Chem.* **2013**, *52*, 5201–5205.

(45) Gaviglio, C.; Pellegrino, J.; Milstein, D.; Doctorovich, F. NO disproportionation by a {RhNO}<sup>9</sup> pincer-type complex. *Dalton Trans.* **2017**, *46*, 16878–16884.

(46) Gwak, J.; Ahn, S.; Baik, M.-H.; Lee, Y. One metal is enough: a nickel complex reduces nitrate anions to nitrogen gas. *Chem. Sci.* **2019**, *10*, 4767–4774.

(47) Tao, W.; Bower, J. K.; Moore, C. E.; Zhang, S. Dicopper-μ-Oxo, μ-Nitrosyl Complex from the Activation of NO or Nitrite at a Dicopper Center. *J. Am. Chem. Soc.* **2019**, *141*, 10159–10164.

(48) Bau, R.; Sabherwal, I. H.; Burg, A. B. Preparation and Structure of Co<sub>4</sub>(NO)<sub>8</sub>(NO<sub>2</sub>)<sub>2</sub>(N<sub>2</sub>O<sub>2</sub>). Novel Complex Containing a Quadridentate Hyponitrite Group. *J. Am. Chem. Soc.* **1971**, *93*, 4926–4928.

(49) Lu, T.-T.; Wang, Y.-M.; Hung, C.-H.; Chiou, S.-J.; Liaw, W.-F. Bioinorganic Chemistry of the Natural [Fe(NO)<sub>2</sub>]<sup>9</sup> Motif: Evolution of a Functional Model for NO-Related Biomedical Application and Revolutionary Development of a Translational Model. *Inorg. Chem.* **2018**, *57*, 12425–12443.

(50) Toledo, J. C., Jr.; Bosworth, C. A.; Hennon, S. W.; Mahtani, H. A.; Bergonia, H. A.; Lancaster, J. R., Jr. Nitric oxide-induced conversion of cellular chelatable iron into macromolecule-bound paramagnetic dinitrosyliron complexes. *J. Biol. Chem.* **2008**, *283*, 28926–28933.

(51) Hsiao, H.-Y.; Chung, C.-W.; Santos, J. H.; Villaflores, O. B.; Lu, T.-T. Fe in biosynthesis, translocation, and signal transduction of NO: toward bioinorganic engineering of dinitrosyl iron complexes into NO-delivery scaffolds for tissue engineering. *Dalton Trans.* **2019**, *48*, 9431–9453.

(52) Lehnert, N.; Fujisawa, K.; Camarena, S.; Dong, H. T.; White, C. J. Activation of Non-Heme Iron-Nitrosyl Complexes: Turning Up the Heat. *ACS Catal.* **2019**, *9*, 10499–10518.

(53) Bello, M. L.; Nuccetelli, M.; Caccuri, A. M.; Stella, L.; Parker, M. W.; Rossjohn, J.; McKinstry, W. J.; Mozzi, A. F.; Federici, G.;

Polizio, F.; Pedersen, J. Z.; Ricci, G. Human glutathione transferase P1–1 and nitric oxide carriers; a new role for an old enzyme. *J. Biol. Chem.* **2001**, *276*, 42138–42145.

(54) Cesareo, E.; Parker, L. J.; Pedersen, J. Z.; Nuccetelli, M.; Mazzetti, A. P.; Pastore, A.; Federici, G.; Caccuri, A. M.; Ricci, G.; Adams, J. J.; Parker, M. W.; Bello, M. L. Nitrosylation of human glutathione transferase P1–1 with dinitrosyl diglutathionyl iron complex in vitro and in vivo. *J. Biol. Chem.* **2005**, *280*, 42172–42180.

(55) Watts, R. N.; Hawkins, C.; Ponka, P.; Richardson, D. R. Nitrogen monoxide (NO)-mediated iron release from cells is linked to NO-induced glutathione efflux via multidrug resistance-associated protein 1. *Proc. Natl. Acad. Sci. U. S. A.* **2006**, *103*, 7670–7675.

(56) Pedersen, J. Z.; De Maria, F.; Turella, P.; Federici, G.; Mattei, M.; Fabrini, R.; Dawood, K. F.; Massimi, M.; Caccuri, A. M.; Ricci, G. Glutathione transferases sequester toxic dinitrosyl-iron complexes in cells. A protection mechanism against excess nitric oxide. *J. Biol. Chem.* **2007**, *282*, 6364–6371.

(57) Lok, H. C.; Sahni, S.; Richardson, V.; Kalinowski, D. S.; Kovacevic, Z.; Lane, D. J.; Richardson, D. R. Glutathione S-transferase and MRP1 form an integrated system involved in the storage and transport of dinitrosyl-dithiolato iron complexes in cells. *Free Radical Biol. Med.* **2014**, *75*, 14–29.

(58) (a) Tsai, M.-L.; Tsou, C.-C.; Liaw, W.-F. Dinitrosyl Iron Complexes (DNICs): From Biomimetic Synthesis and Spectroscopic Characterization toward Unveiling the Biological and Catalytic Roles of DNICs. *Acc. Chem. Res.* **2015**, *48*, 1184–1193. (b) Darensbourg, M. Y.; Pulkukody, R. Synthetic Advances Inspired by the Bioactive Dinitrosyl Iron Unit. *Acc. Chem. Res.* **2015**, *48*, 2049–2058.

(59) Ke, C.-H.; Chen, C.-H.; Tsai, M.-L.; Wang, H.-C.; Tsai, F.-T.; Chiang, Y.-W.; Shih, W.-C.; Bohle, D. S.; Liaw, W.-F. {Fe(NO)<sub>2</sub>}<sup>9</sup> Dinitrosyl Iron Complex Acting as a Vehicle for the NO Radical. *J. Am. Chem. Soc.* **2017**, *139*, 67–70.

(60) (a) Tsai, F.-T.; Kuo, T.-S.; Liaw, W.-F. Dinitrosyl Iron Complexes (DNICs) Bearing O-Bound Nitrito Ligand: Reversible Transformation between the Six-Coordinate {Fe(NO)<sub>2</sub>}<sup>9</sup> [(1-MeIm)<sub>2</sub>(η<sup>2</sup>-ONO)Fe(NO)<sub>2</sub>] (g = 2.013) and Four-Coordinate {Fe(NO)<sub>2</sub>}<sup>9</sup> [(1-MeIm)(ONO)Fe(NO)<sub>2</sub>] (g = 2.03). *J. Am. Chem. Soc.* **2009**, *131*, 3426–3427. (b) Tsai, F.-T.; Chen, P.-L.; Liaw, W.-F. Roles of the Distinct Electronic Structures of the {Fe(NO)<sub>2</sub>}<sup>9</sup> and {Fe(NO)<sub>2</sub>}<sup>10</sup> Dinitrosyliron Complexes in Modulating Nitrite Binding Modes and Nitrite Activation Pathways. *J. Am. Chem. Soc.* **2010**, *132*, 5290–5299.

(61) Tsai, F.-T.; Lee, Y.-C.; Chiang, M.-H.; Liaw, W.-F. Nitrate-to-Nitrite-to-Nitric Oxide Conversion Modulated by Nitrate-Containing {Fe(NO)<sub>2</sub>}<sup>9</sup> Dinitrosyl Iron Complex (DNIC). *Inorg. Chem.* **2013**, *52*, 464–473.

(62) Tseng, Y.-T.; Ching, W.-M.; Liaw, W.-F.; Lu, T.-T. Dinitrosyl Iron Complex [K-18-crown-6-ether][(NO)<sub>2</sub>Fe<sup>(Me)PyrCO<sub>2</sub>}]<sup>9</sup>: Intermediate for Capture and Reduction of Carbon Dioxide. *Angew. Chem.* **2020**, *132*, 11917–11921.</sup>

(63) Speelman, A. L.; Zhang, B.; Silakov, A.; Skodje, K. M.; Alp, E. E.; Zhao, J.; Hu, M. Y.; Kim, E.; Krebs, C.; Lehnert, N. Unusual Synthetic Pathway for an {Fe(NO)<sub>2</sub>}<sup>9</sup> Dinitrosyl Iron Complex (DNIC) and Insight into DNIC Electronic Structure via Nuclear Resonance Vibrational Spectroscopy. *Inorg. Chem.* **2016**, *55*, 5485–5501.

(64) Reginato, N.; McCrory, C. T. C.; Pervitsky, D.; Li, L. Synthesis, X-ray Crystal Structure, and Solution Behavior of Fe(NO)<sub>2</sub>(1-MeIm)<sub>2</sub>: Implications for Nitrosyl Non-Heme-Iron Complexes with g = 2.03. *J. Am. Chem. Soc.* **1999**, *121*, 10217–10218.

(65) Hung, M.-C.; Tsai, M.-C.; Lee, G.-H.; Liaw, W.-F. Transformation and Structural Discrimination between the Neutral {Fe(NO)<sub>2</sub>}<sup>10</sup> Dinitrosyliron Complexes (DNICs) and the Anionic/Cationic {Fe(NO)<sub>2</sub>}<sup>9</sup> DNICs. *Inorg. Chem.* **2006**, *45*, 6041–6047.

(66) Tsai, M.-L.; Hsieh, C.-H.; Liaw, W.-F. Dinitrosyl Iron Complexes (DNICs) Containing S/N/O Ligation: Transformation of Roussin's Red Ester into the Neutral {Fe(NO)<sub>2</sub>}<sup>10</sup> DNICs. *Inorg. Chem.* **2007**, *46*, 5110–5117.

- (67) Tsou, C.-C.; Lu, T.-T.; Liaw, W.-F. EPR, UV–Vis, IR, and X-ray Demonstration of the Anionic Dimeric Dinitrosyl Iron Complex  $[(\text{NO})_2\text{Fe}(\mu\text{-S}^t\text{Bu})_2\text{Fe}(\text{NO})_2]^-$ : Relevance to the Products of Nitrosylation of Cytosolic and Mitochondrial Aconitases, and High-Potential Iron Proteins. *J. Am. Chem. Soc.* **2007**, *129*, 12626–12627.
- (68) Chen, Y.-J.; Ku, W.-C.; Feng, L.-T.; Tsai, M.-L.; Hsieh, C.-H.; Hsu, W.-H.; Liaw, W.-F.; Hung, C.-H.; Chen, Y.-J. Nitric Oxide Physiological Responses and Delivery Mechanisms Probed by Water-Soluble Roussin's Red Ester and  $\{\text{Fe}(\text{NO})_2\}^{10}$  DNIC. *J. Am. Chem. Soc.* **2008**, *130*, 10929–10938.
- (69) Lu, T.-T.; Chen, C.-H.; Liaw, W.-F. Formation of the Distinct Redox-Interrelated Forms of Nitric Oxide from Reaction of Dinitrosyl Iron Complexes (DNICs) and Substitution Ligands. *Chem. - Eur. J.* **2010**, *16*, 8088–8095.
- (70) Shih, W. C.; Lu, T. T.; Yang, L. B.; Tsai, F. T.; Chiang, M. H.; Lee, J. F.; Chiang, Y. W.; Liaw, W. F. New Members of a Class of Dinitrosyliron Complexes (DNICs): The Characteristic EPR Signal of the Six-Coordinate and Five-Coordinate  $\{\text{Fe}(\text{NO})_2\}^9$  DNICs. *J. Inorg. Biochem.* **2012**, *113*, 83–93.
- (71) Tsou, C.-C.; Tsai, F.-T.; Chen, H.-Y.; Hsu, I. J.; Liaw, W.-F. Insight into One-Electron Oxidation of the  $\{\text{Fe}(\text{NO})_2\}^9$  Dinitrosyl Iron Complex (DNIC): Aminyl Radical Stabilized by  $[\text{Fe}(\text{NO})_2]$  Motif. *Inorg. Chem.* **2013**, *52*, 1631–1639.
- (72) Lu, T.-T.; Huang, H.-W.; Liaw, W.-F. Anionic Mixed Thiolate–Sulfide-Bridged Roussin's Red Esters  $[(\text{NO})_2\text{Fe}(\mu\text{-SR})(\mu\text{-S})\text{Fe}(\text{NO})_2]^-$  (R = Et, Me, Ph): A Key Intermediate for Transformation of Dinitrosyl Iron Complexes (DNICs) to  $[2\text{Fe}-2\text{S}]$  Clusters. *Inorg. Chem.* **2009**, *48*, 9027–9035.
- (73) Yeh, S.-W.; Lin, C.-W.; Liu, B.-H.; Tsou, C.-C.; Tsai, M.-L.; Liaw, W.-F. Chelate-Thiolate-Coordinate Ligands Modulating the Configuration and Electrochemical Property of Dinitrosyliron Complexes (DNICs). *Chem. - Eur. J.* **2015**, *21*, 16035–16046.
- (74) Yeh, S.-W.; Lin, C.-W.; Li, Y.-W.; Hsu, I. J.; Chen, C.-H.; Jang, L.-Y.; Lee, J.-F.; Liaw, W.-F. Insight into the Dinuclear  $\{\text{Fe}(\text{NO})_2\}^{10}$ - $\{\text{Fe}(\text{NO})_2\}^{10}$  and Mononuclear  $\{\text{Fe}(\text{NO})_2\}^{10}$  Dinitrosyl iron Complexes. *Inorg. Chem.* **2012**, *51*, 4076–4087.
- (75) Tsai, M.-C.; Tsai, F.-T.; Lu, T.-T.; Tsai, M.-L.; Wei, Y.-C.; Hsu, I. J.; Lee, J.-F.; Liaw, W.-F. Relative Binding Affinity of Thiolate, Imidazole, Phenoxide, and Nitrite Toward the  $\{\text{Fe}(\text{NO})_2\}$  Motif of Dinitrosyl Iron Complexes (DNICs): The Characteristic Pre-Edge Energy of  $\{\text{Fe}(\text{NO})_2\}^9$  DNICs. *Inorg. Chem.* **2009**, *48*, 9579–9591.
- (76) Liu, P.-H.; Tsai, F.-T.; Chen, B.-H.; Hsu, I.-J.; Hsieh, H.-H.; Liaw, W.-F. Insight into Chalcogenolate-Bound  $\{\text{Fe}(\text{NO})_2\}^9$  Dinitrosyl Iron Complexes (DNICs): Covalent Character versus Ionic Character. *Dalton Trans.* **2019**, *48*, 6040–6050.
- (77) Chiang, C.-K.; Chu, K.-T.; Lin, C.-C.; Xie, S.-R.; Liu, Y.-C.; Demeshko, S.; Lee, G.-H.; Meyer, F.; Tsai, M.-L.; Chiang, M.-H.; Lee, C.-M. Photoinduced NO and HNO Production from Mononuclear  $\{\text{FeNO}\}^6$  Complex Bearing a Pendant Thiol. *J. Am. Chem. Soc.* **2020**, *142*, 8649–8661.
- (78) (a) Sheldrick, G. M. *SADABS, Siemens Area Detector Absorption Correction Program*; University of Göttingen: Germany, 1996. (b) North, A. C. T.; Phillips, D. C.; Mathews, F. S. A semi-empirical method of absorption correction. *Acta Crystallogr., Sect. A: Cryst. Phys., Diffraction, Theor. Gen. Crystallogr.* **1968**, *A24*, 351–359.
- (79) Sheldrick, G. M. *SHELXTL: A Program for Crystal Structure Determination*; Siemens Analytical X-ray Instruments, Inc.: Madison, WI, 1994.
- (80) (a) Bain, G. A.; Berry, J. F. Diamagnetic Corrections and Pascal's Constants. *J. Chem. Educ.* **2008**, *85*, 532–536. (b) Kahn, O. *Molecular Magnetism*; VCH Publishers: New York, 1993.
- (81) (a) Glaser, T.; Hedman, B.; Hodgson, K. O.; Solomon, E. I. Ligand K-Edge X-ray Absorption Spectroscopy: A Direct Probe of Ligand–Metal Covalency. *Acc. Chem. Res.* **2000**, *33*, 859–868. (b) Solomon, E. I.; Hedman, B.; Hodgson, K. O.; Dey, A.; Szilagyi, R. K. Ligand K-edge x-ray absorption spectroscopy: Covalency of ligand-metal bonds. *Coord. Chem. Rev.* **2005**, *249*, 97–129. (c) Rose, K.; Shadle, S. E.; Eidsness, M. K.; Kurtz, D. M., Jr.; Scott, R. A.; Hedman, B.; Hodgson, K. O.; Solomon, E. I. Investigation of Iron–Sulfur Covalency in Rubredoxins and a Model System Using Sulfur K-Edge X-ray Absorption Spectroscopy. *J. Am. Chem. Soc.* **1998**, *120*, 10743–10747.
- (82) Schäfer, A.; Huber, C.; Ahlrichs, R. Fully optimized contracted Gaussian basis sets of triple zeta valence quality for atoms Li to Kr. *J. Chem. Phys.* **1994**, *100*, 5829.
- (83) Hehre, W. J.; Ditchfield, R.; Pople, J. A. Self-Consistent Molecular Orbital Methods. XII. Further Extensions of Gaussian—Type Basis Sets for Use in Molecular Orbital Studies of Organic Molecules. *J. Chem. Phys.* **1972**, *56*, 2257.
- (84) Frisch, M. J.; Trucks, G. W.; Schlegel, H. B.; Scuseria, G. E.; Robb, M. A.; Cheeseman, J. R.; Scalmani, G.; Barone, V.; Petersson, G. A.; Nakatsuji, H.; Li, X.; Caricato, M.; Marenich, A. V.; Bloino, J.; Janesko, B. G.; Gomperts, R.; Mennucci, B.; Hratchian, H. P.; Ortiz, J. V.; Izmaylov, A. F.; Sonnenberg, J. L.; D., Williams-Young, Ding, F.; Lipparini, F.; Egidi, F.; Goings, J.; Peng, B.; Petrone, A.; Henderson, T.; Ranasinghe, D.; Zakrzewski, V. G.; Gao, J.; Rega, N.; Zheng, G.; Liang, W.; Hada, M.; Ehara, M.; Toyota, K.; Fukuda, R.; Hasegawa, J.; Ishida, M.; Nakajima, T.; Honda, Y.; Kitao, O.; Nakai, H.; Vreven, T.; Throssell, K.; Montgomery, J. A., Jr.; Peralta, J. E.; Ogliaro, F.; Bearpark, M. J.; Heyd, J. J.; Brothers, E. N.; Kudin, K. N.; Staroverov, V. N.; Keith, T. A.; Kobayashi, R.; Normand, J.; Raghavachari, K.; Rendell, A. P.; Burant, J. C.; Iyengar, S. S.; Tomasi, J.; Cossi, M.; Millam, J. M.; Klene, M.; Adamo, C.; Cammi, R.; Ochterski, J. W.; Martin, R. L.; Morokuma, K.; Farkas, O.; Foresman, J. B.; Fox, D. J. *Gaussian 16*, revision B.01, Gaussian, Inc.: Wallingford, CT, 2016.
- (85) Staroverov, V. N.; Scuseria, G. E.; Tao, J.; Perdew, J. P. Comparative Assessment of a New Nonempirical Density Functional: Molecules and Hydrogen-Bonded Complexes. *J. Chem. Phys.* **2003**, *119*, 12129–12137.
- (86) (a) Miertuš, S.; Scrocco, E.; Tomasi, J. Electrostatic interaction of a solute with a continuum. A direct utilization of AB initio molecular potentials for the prevision of solvent effects. *Chem. Phys.* **1981**, *55*, 117. (b) Miertus, S.; Tomasi, J. Approximate evaluations of the electrostatic free energy and internal energy changes in solution processes. *Chem. Phys.* **1982**, *65*, 239. (c) Cossi, M.; Barone, V.; Cammi, R.; Tomasi, J. Ab initio study of solvated molecules: a new implementation of the polarizable continuum model. *Chem. Phys. Lett.* **1996**, *255*, 327. (d) Tomasi, J.; Mennucci, B.; Cammi, R. Quantum mechanical continuum solvation models. *Chem. Rev.* **2005**, *105*, 2999.
- (87) Grimme, S.; Ehrlich, S.; Goerigk, L. Effect of the damping function in dispersion corrected density functional theory. *J. Comput. Chem.* **2011**, *32*, 1456.
- (88) Glendening, E. D.; Reed, A. E.; Carpenter, J. E.; Weinhold, F. *NBO*, version 3.1.; Gaussian Inc.: Pittsburgh, 2003.
- (89) *Avogadro: An Open-Source Molecular Builder and Visualization Tool*, version 1.1.1; <http://avogadro.openmolecules.net/>.